

Superfluidity of Dirac Fermions in a Tunable Honeycomb Lattice: Cooper Pairing, Collective Modes, and Critical Currents

Shunji Tsuchiya,^{1,2} R. Ganesh,³ and Arun Paramekanti^{4,5}

¹*Department of Physics, Faculty of Science, Tokyo University of Science,
1-3 Kagurazaka, Shinjuku-ku, Tokyo 162-8601, Japan*

²*Research and Education Center for Natural Sciences,
Keio University, 4-1-1 Hiyoshi, Kanagawa 223-8521, Japan*

³*Institute for Theoretical Solid State Physics, IFW Dresden, Helmholtzstr. 20, 01069 Dresden, Germany*

⁴*Department of Physics, University of Toronto, Toronto, Ontario, M5S 1A7, Canada*

⁵*Canadian Institute for Advanced Research, Toronto, Ontario, M5S 1A7, Canada*

(Dated: December 3, 2024)

Motivated by recent experiments on atomic Dirac fermions in a tunable honeycomb optical lattice, we study the attractive Hubbard model of superfluidity in the anisotropic honeycomb lattice. At weak-coupling, we find that the maximum mean field pairing transition temperature, as a function of density and interaction strength, occurs for the case with isotropic hopping amplitudes. In this isotropic case, we go beyond mean field theory and study collective fluctuations, treating both pairing and density fluctuations for interaction strengths ranging from weak to strong coupling. We find evidence for a sharp sound mode, together with a well-defined Leggett mode over a wide region of the phase diagram. We also calculate the superfluid order parameter and collective modes in the presence of nonzero superfluid flow. We find that the superfluid order parameter and density fluctuations exhibit nontrivial dependence on superflow. The softening of these collective modes leads to dynamical instabilities involving stripe-like density modulations as well as a Leggett-mode instability associated with the natural sublattice symmetry breaking charge-ordered state on the honeycomb lattice. We delineate regimes of the phase diagram where the critical current is limited by depairing or by such collective instabilities, and discuss experimental implications of our results.

PACS numbers: 67.85.Lm,71.10.Fd,81.05.ue,74.70.Wz

I. INTRODUCTION

Ultracold atoms in optical lattices are of great interest for studying strongly correlated states of quantum matter, and such emergent phenomena as superconductivity and magnetism [1, 2]. Stimulated by the discovery of graphene, and ongoing intense research in that field [3], optical lattices with the honeycomb lattice structure are beginning to be explored by various groups [4–6]. In the context of graphene, various exotic phenomena related to massless Dirac fermions as well as interesting topological phases and quantum phase transitions have been widely explored [7–9]. While superconductivity still remains elusive in experiments on graphene, it has been the focus of recent theoretical work suggesting chiral superconductivity induced by repulsive interactions [10–12]. Earlier, motivated by a possible cold atom realization, where the interatomic interaction may be modelled by an s -wave attractive contact potential, the attractive fermion Hubbard model on the two-dimensional (2D) honeycomb lattice was studied and found to exhibit a quantum phase transition at half-filling between semimetal with massless Dirac fermion excitations and a simple s -wave superfluid phase [13, 14]. This quantum phase transition was shown to be the end point (with changing density) of a suitably defined BCS-BEC crossover line away from half filling [14]. This is reminiscent of the manner in which the usual BCS-BEC crossover phenomenon in the continuum in 3D at finite density is linked to the “zero density quantum critical point” associated with two-body bound state formation [15]. The semimetal to superconductor transition found on the honeycomb lattice is the simplest version of more general band insulator to superfluid transitions discussed in experiments [16] and theory [17–20]. The critical theory of this semimetal to superconductor transition is also a topic of great recent interest [21].

In this paper, motivated by the recent experimental developments reported by the ETH group [6], we present a careful study of Cooper pairing, superfluid collective modes, and superflow instabilities which limit the critical current in the attractive Hubbard model on the honeycomb lattice. Our main results, which go beyond previous work on this topic, are as follows. (i) We study the mean field pairing transition temperature T_c^0 in a general *anisotropic* honeycomb lattice as has been realized in a “brick-wall” type geometry in the ETH experiments [6], with hoppings as shown in Fig. 1. For weak coupling, the maximum T_c^0 , as a function of fermion density and interaction strength, is found to occur in the isotropic limit. We then argue more generally that the vicinity of this isotropic point, with all hoppings being equal, is the most promising limit to experimentally explore the superfluidity of atomic fermions. (ii) In this limit of isotropic hopping, we compute the collective modes in the superfluid, treating both density and phase fluctuations on equal footing in contrast to previous work which only studied superconducting fluctuations [14].

We find evidence for the expected sharp Anderson-Bogoliubov (AB) sound mode; in addition, over a wide swath of the phase diagram, we uncover a well-defined Leggett mode, which involves intra-unit-cell coupled oscillations of the density and superfluid order parameter phase. (iii) Imposing a nonzero superflow, we find that the superfluid phase becomes unstable via either a depairing instability or collective charge modulational instabilities driven by a softening of the collective mode spectrum. The superfluid is most stable against depairing in the vicinity of special fillings associated with van Hove (vH) singularities in the density of states; in this regime, at mean-field level, we find the emergence of a supercurrent induced gapless superfluid state. The collective charge modulational instabilities that we uncover include tendencies towards forming incommensurate charge orders, stripe-like modulations, or sublattice symmetry breaking charge density wave order (CDW). Aside from the depairing instability, which occurs primarily at small fermion density or in the weak attraction limit, we expect such *collective instabilities* to limit the critical current in this system. In fact, the current-induced gapless superfluid state we uncover in mean-field theory is preempted by such collective dynamical or Landau instabilities. Furthermore, the sublattice CDW order or the instability associated with this CDW order arises from a subtle pseudospin SU(2) symmetry of the attractive Hubbard model at half filling; probing for such CDW order could thus also serve as an indirect diagnostic that the attractive one band Hubbard model is an appropriate description of the low energy physics in a deep optical lattice. Our predictions could be tested by using Bragg scattering experiments to study the collective mode spectrum.

The results described above are obtained using a generalized random phase approximation (GRPA) complemented by strong coupling “pseudospin”-wave theory where appropriate. Our work here builds on similar previous studies addressing the collective modes and critical current limiting instabilities on square and cubic optical lattices [22–24]. In those cases, it has been shown that the collective mode spectrum of *s*-wave superfluids exhibits, in addition to the long wavelength AB sound mode, a sharp ‘roton minimum’ near the corner of the Brillouin zone (BZ) due to strong charge density wave fluctuations, and ‘roton mode softening’ leads to a collective dynamical instability of superflow.

This paper is organized as follows. In Sec. II, we first examine the honeycomb optical lattice setup from Ref. [6] which can tune the anisotropy of Dirac cones, and discuss the mean field T_c as a function of anisotropy λ , interaction U , and filling n . In Sec. III, we calculate the superfluid order parameter and quasiparticle dispersion in the presence of superflow. Sec. IV uses the GRPA to compute the spectrum of collective excitations as a function of flow. In the strong coupling limit, this section compares the GRPA result with a spin wave expansion of the appropriate pseudospin Hamiltonian. GRPA works well even at strong coupling, as it shows excellent agreement with spin wave theory. This method agrees with the GRPA result giving us confidence that GRPA works well even in the strong coupling limit. Finally, Sec. IV B discusses the different kinds of superflow instabilities as a function of density and interaction strength. We find a dynamical instability at the Γ point which arises from competing CDW order. In addition, we find an unexpected stripe-like instability which persists even in the strong coupling limit. We conclude by discussing implications for experiments.

II. HONEYCOMB LATTICE WITH TUNABLE ANISOTROPY

The experiments by Tarruell, et al. [6], realize a tunable optical lattice which could be viewed as a “brick-wall” lattice or an anisotropic honeycomb lattice. In a deep optical lattice, we can restrict attention to the lowest band and work with a single band tight-binding model. On symmetry grounds, two of the three nearest neighbor hoppings on this lattice are equivalent in the experiments, so we denote the three hopping amplitudes by $(t, t, \lambda t)$ as shown in Fig. 1 (a). In the experiments, one pair of sites can be made closer to each other, so we expect $\lambda \geq 1$. Here, however, we will also study the case $\lambda < 1$ at mean field level.

A. Attractive Hubbard model

Since future experiments are likely to be able to study atomic fermions with attractive interactions in this lattice, we consider the attractive Hubbard model on this anisotropic honeycomb lattice as a reasonable starting point to study the superfluid phase. The Hamiltonian is thus given by

$$H = - \sum_{\langle i,j \rangle, \sigma} t_{ij} \left(c_{i\sigma}^\dagger c_{j\sigma} + c_{j\sigma}^\dagger c_{i\sigma} \right) - \mu \sum_{i,\sigma} n_{i\sigma} - U \sum_i n_{i\uparrow} n_{i\downarrow}. \quad (1)$$

where $c_{j\sigma}^\dagger$ is the creation operator of a fermion with spin σ ($=\uparrow, \downarrow$) at site j , $\langle i, j \rangle$ correspond to nearest neighbor sites coupled by a hopping amplitude t_{ij} , the chemical potential μ tunes the fermion density, and U is the local Hubbard attraction. The hopping $t_{ij} = (t, t, \lambda t)$ is chosen as shown in Fig. 1 (a) for the three neighboring sites.

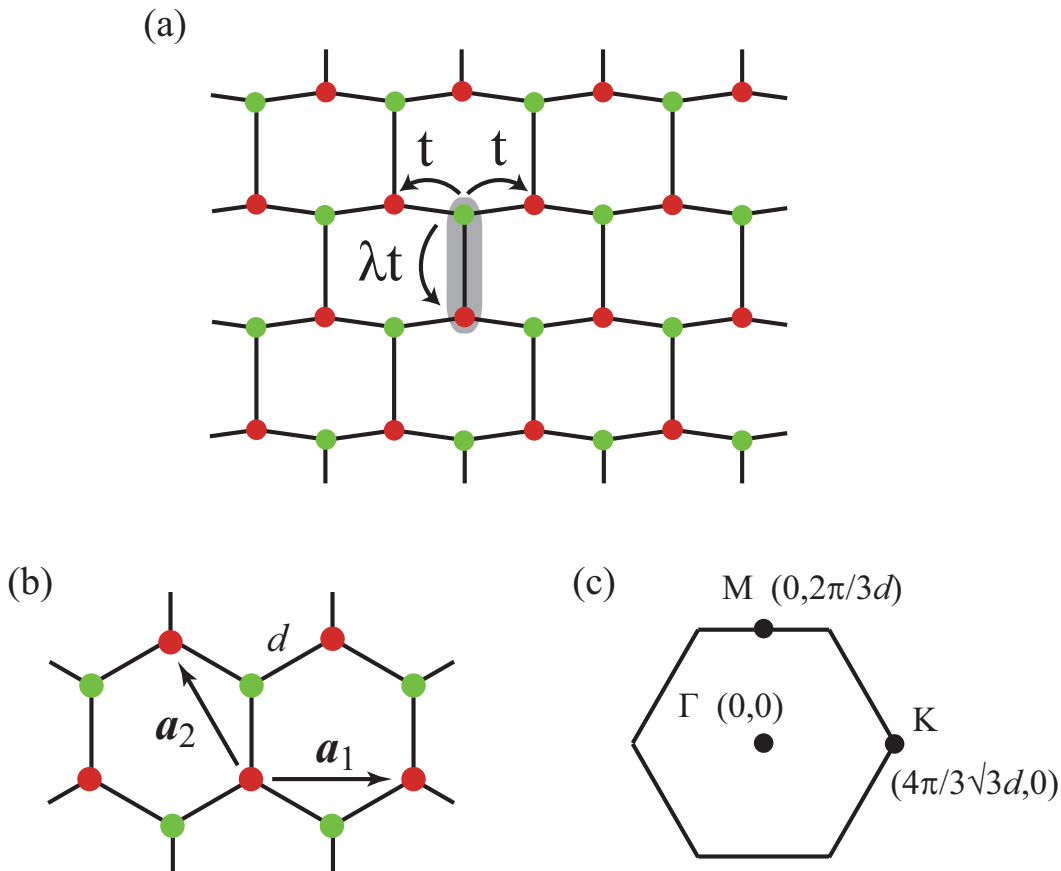


FIG. 1: (Color online) (a) Honeycomb lattice in a “brick-wall” type geometry. Sites of the A(B) sublattice are shown in red(green). Asymmetric hopping amplitudes are captured by a parameter λ . $\lambda = 1$ is the isotropic limit. The shaded area shows the unit cell. (b) Honeycomb lattice with primitive lattice vectors. (c) The Brillouin zone with the high symmetry points indicated.

B. Single-particle dispersion

The single-particle Hamiltonian in momentum space takes the form

$$H = \sum_{\mathbf{k}, \sigma} \left(\gamma_{\mathbf{k}} c_{\mathbf{k}, a, \sigma}^{\dagger} c_{\mathbf{k}, b, \sigma} + \gamma_{\mathbf{k}}^* c_{\mathbf{k}, b, \sigma}^{\dagger} c_{\mathbf{k}, a, \sigma} \right) \quad (2)$$

where the subscripts a, b refer to the two sublattices, and

$$\gamma_{\mathbf{k}} = -t(\lambda + e^{i\mathbf{k} \cdot \mathbf{a}_2} + e^{i\mathbf{k} \cdot (\mathbf{a}_1 + \mathbf{a}_2)}), \quad (3)$$

with $\mathbf{a}_1 = (\sqrt{3}d, 0)$ and $\mathbf{a}_2 = (-\sqrt{3}d/2, 3d/2)$ are the two basis vectors shown in Fig. 1 (b). This results in two dispersing bands with energies $\pm|\gamma_{\mathbf{k}}|$.

For $U = 0$, we plot the noninteracting band dispersion $|\gamma_{\mathbf{k}}|$ for three different values of λ as shown in Fig. 2. In the isotropic limit, $\lambda = 1$, there are two zero energy Dirac cones which occur at the K points (BZ corners) as is familiar from graphene. Upon decreasing λ from unity, the two Dirac points move towards the Γ point. When $\lambda \ll 1$, the system becomes quasi one dimensional and the Dirac points acquire highly anisotropic velocities, with a smaller velocity along the \hat{y} direction. For $\lambda > 1$, increasing λ moves the Dirac cones along the BZ edge towards the M point (edge center), with a concomitant tunable velocity anisotropy. Eventually, at $\lambda = 2$, the two Dirac points meet at the M point and subsequently ‘annihilate’ each other, resulting in a gapped spectrum [25–27]. Such moving and merging/gapping of Dirac points have been observed in the ETH experiments [6].

Figure 3 shows the density of states (DOS) at the Fermi level as a function of λ and fermion filling n (here $n = 1$ corresponds to ‘half filling’ with one fermion on average per lattice site). In the isotropic $\lambda = 1$ limit, the DOS exhibits vH singularities at $n = 3/4, 5/4$ arising from the hexagonal shape of the Fermi surface at these densities.

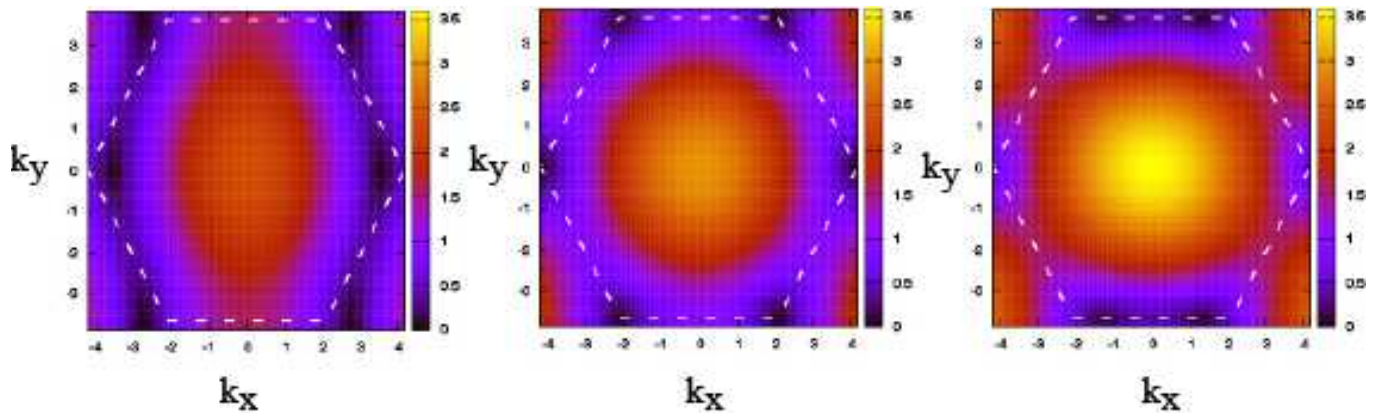


FIG. 2: (Color online) Top view of dispersion of the non-interacting electrons with $\lambda = 0.4$ (left), $\lambda = 1$ (centre), and $\lambda = 1.6$ (right). The white dashed line is the boundary of the first Brillouin zone. In the symmetric $\lambda = 1$ limit, the Dirac cones lie at the K points.

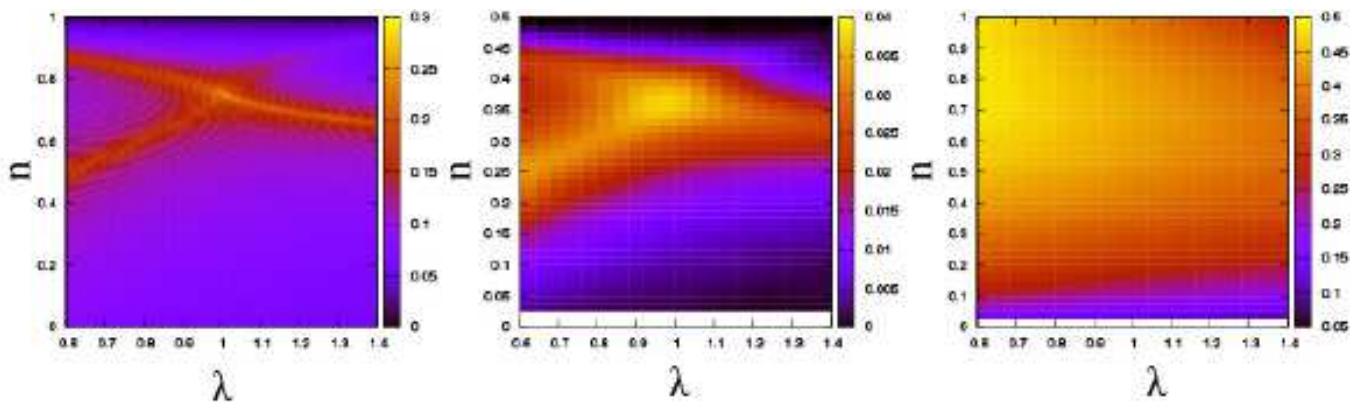


FIG. 3: (Color online) Left: $g(\epsilon_F)$, density of states at the Fermi level as a function of filling and λ . We only show $n < 1$ as the system is particle-hole symmetric. Centre: Mean-field T_c/t with $U/t = 1$ as a function of filling (in units of fermions per site) and λ . Right: Mean-field T_c/t with $U/t = 3$ as a function of filling (in units of fermions per site) and λ .

Upon decreasing λ from unity, we find that these vH peaks split into two branches. As we approach the $\lambda = 0$ limit, one of the branches merges with the ‘band edge’ at $n = 0$ or $n = 2$. The other branch approaches $n = 1$, however it gets weaker and eventually vanishes at $\lambda = 0$. Upon increasing λ from unity, we again find that the vH singularities at $n = 3/4, 5/4$ split into two branches. For $\lambda \gg 1$, the DOS peaks at densities $n = 0, 2$, at energies $\pm\lambda t$ corresponding to the bonding and antibonding state energies of isolated strong bonds.

C. Cooper pairing: Mean-field theory

We next consider the effect of the attractive Hubbard interaction. At mean-field level, the ground state of this model is generically a superfluid state formed by condensing Cooper pairs. To study this superfluid state, the fermions have to be cooled (at least) below the mean field transition temperature, T_c^0 , corresponding to the onset of Cooper pairing. We therefore begin by examining T_c^0 as a function of anisotropy λ , and filling.

At mean field level, the gap and number equations are given by [14]

$$\frac{1}{U} = \frac{1}{N} \sum_{\mathbf{k}} \sum_{\tau=\pm} \frac{\tanh \frac{\beta E_{\tau}(\mathbf{k})}{2}}{2E_{\tau}(\mathbf{k})}. \quad (4)$$

and

$$n = 1 - \frac{1}{N} \sum_{\mathbf{k}} \sum_{\tau=\pm} \frac{\xi_{\mathbf{k}}^{\tau}}{E^{\tau}(\mathbf{k})} \tanh \frac{\beta E^{\tau}(\mathbf{k})}{2}, \quad (5)$$

respectively, where $\xi_{\mathbf{k}}^{\pm} = \pm|\gamma_{\mathbf{k}}| - \mu$ and $E^{\pm}(\mathbf{k}) = \sqrt{(\xi_{\mathbf{k}}^{\pm})^2 + \Delta_0^2}$ (τ denotes the energy bands). $N = 2M$ is the number of lattice sites and M is the number of unit cells. The derivation of Eqs. (4) and (5) is summarized in Appendix A. To determine T_c^0 (and the appropriate μ), we set $\Delta_0 \rightarrow 0$ and $\beta \rightarrow 1/T_c^0$ in these equations and solve them self-consistently.

Within weak-coupling BCS theory, the pairing gap and T_c^0 are determined by $g(\epsilon_F)$, the DOS at the Fermi level in the non-interacting problem. We therefore compare the behavior of the mean-field T_c^0 with the trends in $g(\epsilon_F)$. At weak coupling ($U/t = 1$), we find that the maximum T_c^0 tracks $g(\epsilon_F)$ for all values of lambda and filling as seen from Fig. 3. As seen in the figure, the strong vH singularity in the symmetric $\lambda = 1$ limit, leads to particularly robust T_c^0 in this isotropic case for $n = 3/4, 5/4$. (We will revisit this robustness of the superfluidity in Sec.III B in the context of imposed superflow.) For intermediate and large U/t , the pairing is no longer directly restricted to electrons near the Fermi surface, and the T_c^0 values are no longer governed simply by $g(\epsilon_F)$ as shown in Fig. 3(right). We find that for *all* interaction strengths, the mean-field T_c^0 is highest when $\lambda \leq 1$ as seen from Fig. 3. However, as the system becomes increasingly quasi-1D with decreasing λ , we expect enhanced quantum and thermal fluctuations beyond mean-field theory to suppress superfluidity, especially in the strong coupling regime where the superfluid to normal transition temperature is essentially controlled by fluctuation effects, and not by pair breaking effects which set T_c^0 . On these grounds, we expect the highest superfluid transition temperature to occur in the vicinity of the isotropic limit $\lambda = 1$. We suggest that $\lambda = 1$ and $n = 3/4$ (or $5/4$) is an optimal parameter regime for studying superfluid order in the experiments. In the rest of this paper, we therefore set $\lambda = 1$ and study the collective excitations and superflow instabilities of the resulting superfluid state.

III. NONZERO SUPERFLOW: MEAN FIELD THEORY ON THE ISOTROPIC HONEYCOMB LATTICE

We next turn to the mean field theory of the isotropic honeycomb lattice Hubbard model in the presence of a nonzero superfluid current obtained by considering Cooper pairs with nonzero center of mass momentum \mathbf{Q} . This will allow us to comment on the stability of the superfluid towards depairing (pair breaking) effects. This will also set the stage for the analysis of collective modes and collective mode driven instabilities discussed in later sections.

A. Mean-field theory in the presence of superfluid flow

The order parameter in the presence of superfluid flow with mass momentum \mathbf{Q} is given by

$$\begin{aligned} \Delta_{\mathbf{Q},\nu} e^{i\mathbf{Q}\cdot\mathbf{r}_l} &= U \langle c_{l,\nu,\downarrow} c_{l,\nu,\uparrow} \rangle \\ &= \frac{U}{M} \sum_{\mathbf{k}} \langle c_{-\mathbf{k}+\mathbf{Q}/2,\nu,\downarrow} c_{\mathbf{k}+\mathbf{Q}/2,\nu,\uparrow} \rangle e^{i\mathbf{Q}\cdot\mathbf{r}_l}, \end{aligned} \quad (6)$$

where l denotes unit cell and $\nu(= a, b)$ labels sublattice. Within the mean-field approximation, the Hamiltonian takes the form

$$H = \sum_{\mathbf{k}} \Psi_{\mathbf{Q}}^{\dagger}(\mathbf{k}) \hat{h}_{\mathbf{Q}} \Psi_{\mathbf{Q}}(\mathbf{k}) + \frac{M}{U} \sum_{\nu} |\Delta_{\mathbf{Q},\nu}|^2, \quad (7)$$

where

$$\Psi_{\mathbf{Q}}(\mathbf{k}) = \begin{pmatrix} c_{\mathbf{k}_+,a,\uparrow} \\ c_{\mathbf{k}_-,a,\downarrow} \\ c_{\mathbf{k}_+,b,\uparrow} \\ c_{\mathbf{k}_-,b,\downarrow} \end{pmatrix}, \quad \hat{h}_{\mathbf{Q}} \equiv \begin{pmatrix} -\mu & -\Delta_{\mathbf{Q},a} & \gamma_{\mathbf{k}_+} & 0 \\ -\Delta_{\mathbf{Q},a}^* & \mu & 0 & -\gamma_{\mathbf{k}_-}^* \\ \gamma_{\mathbf{k}_+}^* & 0 & -\mu & -\Delta_{\mathbf{Q},b} \\ 0 & -\gamma_{\mathbf{k}_-} & -\Delta_{\mathbf{Q},b}^* & \mu \end{pmatrix}. \quad (8)$$

Here, \mathbf{k}_\pm denotes $\pm\mathbf{k} + \mathbf{Q}/2$. The matrix \hat{h}_Q can be diagonalized by the Bogoliubov transformation

$$\Psi_Q(\mathbf{k}) = \hat{T}\tilde{\Psi}_Q(\mathbf{k}) = \hat{T} \begin{pmatrix} \alpha_{\mathbf{k},+, \uparrow} \\ \alpha_{-\mathbf{k},+, \downarrow}^\dagger \\ \alpha_{\mathbf{k},-, \uparrow} \\ \alpha_{-\mathbf{k},-, \downarrow}^\dagger \end{pmatrix}, \quad (9)$$

where $\alpha_{\mathbf{k},\tau,\sigma}^\dagger$ is the creation operator of a Bogoliubov quasiparticle with momentum \mathbf{k} , energy band $\tau(=\pm)$, and spin $\sigma(=\uparrow,\downarrow)$. They satisfy the anticommutation relation $\{\alpha_{\mathbf{k},\tau,\sigma}, \alpha_{\mathbf{k}',\tau',\sigma'}^\dagger\} = \delta_{\mathbf{k},\mathbf{k}'}\delta_{\tau,\tau'}\delta_{\sigma,\sigma'}$. The unitary matrix \hat{T} is determined so as to diagonalize the mean-field Hamiltonian

$$H' = \sum_{\mathbf{k}} \Psi_Q^\dagger(\mathbf{k}) \hat{h}_Q \Psi_Q(\mathbf{k}) = \sum_{\mathbf{k}} \tilde{\Psi}_Q^\dagger(\mathbf{k}) \hat{\tilde{h}}_Q \tilde{\Psi}_Q(\mathbf{k}), \quad (10)$$

$$\hat{\tilde{h}}_Q = \hat{T}^\dagger \hat{h}_Q \hat{T} = \begin{pmatrix} E_Q^+(\mathbf{k}) & 0 & 0 & 0 \\ 0 & -E_Q^+(-\mathbf{k}) & 0 & 0 \\ 0 & 0 & E_Q^-(\mathbf{k}) & 0 \\ 0 & 0 & 0 & -E_Q^-(-\mathbf{k}) \end{pmatrix}, \quad (11)$$

where $E_Q^+(\mathbf{k})$ and $E_Q^-(\mathbf{k})$ are the upper and lower quasiparticle energy bands, respectively. Thus, we obtain the diagonalized Hamiltonian

$$H = \sum_{\mathbf{k}} \sum_{\tau=\pm} \left[E_Q^\tau(\mathbf{k}) (\alpha_{\mathbf{k},\tau,\uparrow}^\dagger \alpha_{\mathbf{k},\tau,\uparrow} + \alpha_{\mathbf{k},\tau,\downarrow}^\dagger \alpha_{\mathbf{k},\tau,\downarrow}) - E_Q^\tau(\mathbf{k}) \right] + \frac{M}{U} \sum_{\nu} |\Delta_{Q,\nu}|^2, \quad (12)$$

and the ground state energy

$$E_0 = - \sum_{\mathbf{k}} \sum_{\tau=\pm} E_Q^\tau(\mathbf{k}) + \frac{M}{U} \sum_{\nu} |\Delta_{Q,\nu}|^2. \quad (13)$$

To evaluate $\Delta_{Q,a/b}$ and μ , we solve the corresponding gap and number equations that are explicitly given in Appendix A. The chemical potential is tuned to obtain the required density and the order parameters are chosen to minimize the ground state energy. This scheme is known to interpolate the weak-coupling BCS regime and strong-coupling BEC regime at low temperatures [28–30]. The strong-coupling effect is included in the self-consistently determined chemical potential, which reduces to the Fermi energy in the weak-coupling BCS regime while it deviates from the Fermi energy in the strong coupling BEC regime.

B. Depairing instability and gapless superfluidity

Figure 4 shows the self-consistently calculated order parameter as a function of superflow momentum \mathbf{Q} for different fillings. Hereafter in this section and in Sec. IV, we restrict ourselves at $T = 0$ for simplicity. For any flow direction, we find that the amplitudes of the two order parameters are the same, i.e., $|\Delta_{Q,A}| = |\Delta_{Q,B}| \equiv \Delta_Q$. We plot this amplitude Δ_Q as a function of \mathbf{Q} for different fillings in Fig.4. The Hamiltonian being particle-hole symmetric, we restrict ourselves to densities below half-filling ($n \leq 1$). Sweeping \mathbf{Q} in the BZ, we find that the order parameter generally vanishes discontinuously at some critical flow momentum (except in the vicinity of $n = 3/4$). This depairing instability occurs when the kinetic energy cost of superflow outweighs the energy gain from pairing. The system then reverts to an unpaired normal state via a first order phase transition.

However, when the filling is close to $n = 3/4$ fermions per site, Δ_Q does not vanish for any \mathbf{Q} . This enhanced stability is due to a vH singularity in the non-interacting problem at $n = 3/4$ and $n = 5/4$ (see Fig.3). At these densities, there is a very large density of states at the Fermi level which enhances superfluid order and makes it robust against superflow.

In Fig. 4, each curve for Δ_Q exhibits an interesting *cusplike* structure, at which the derivative $\partial\Delta_Q/\partial\mathbf{Q}$ changes discontinuously. The order parameter starts decreasing rapidly beyond the cusp until the transition to the normal state sets in. This cusp structure signals the onset of *gapless superfluidity*. The evolution of the single-particle spectrum in the lower band $E_Q^-(\mathbf{k})$ is shown in Fig. 5 (a)~(c). With increasing flow, the energy gap to creating quasiparticles decreases for wavevectors in \mathbf{k} in the direction opposite to \mathbf{Q} due to a ‘Doppler shift’ in the dispersion. For large \mathbf{Q} , the gap closes making the single-particle spectrum gapless - this precisely coincides with the cusp feature.

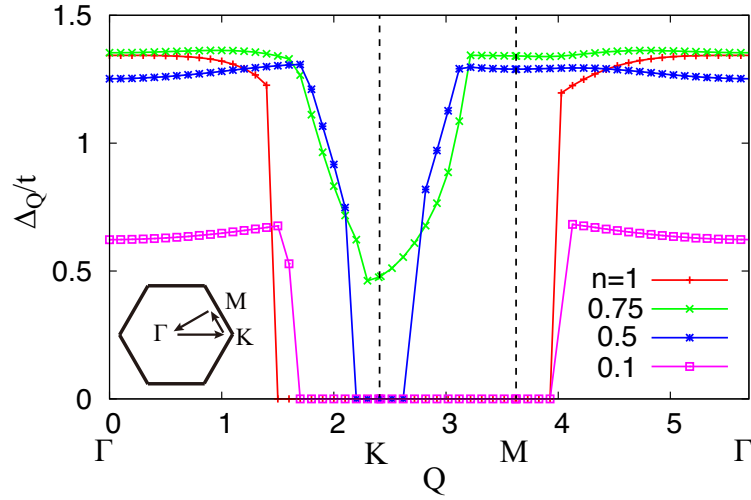


FIG. 4: (Color online) Superfluid order parameter $\Delta_Q (= |\Delta_{Q,a}| = |\Delta_{Q,b}|)$ as a function of the superflow Q for several different fermion fillings at $T = 0$. Q is swept along the contour displayed in the inset.

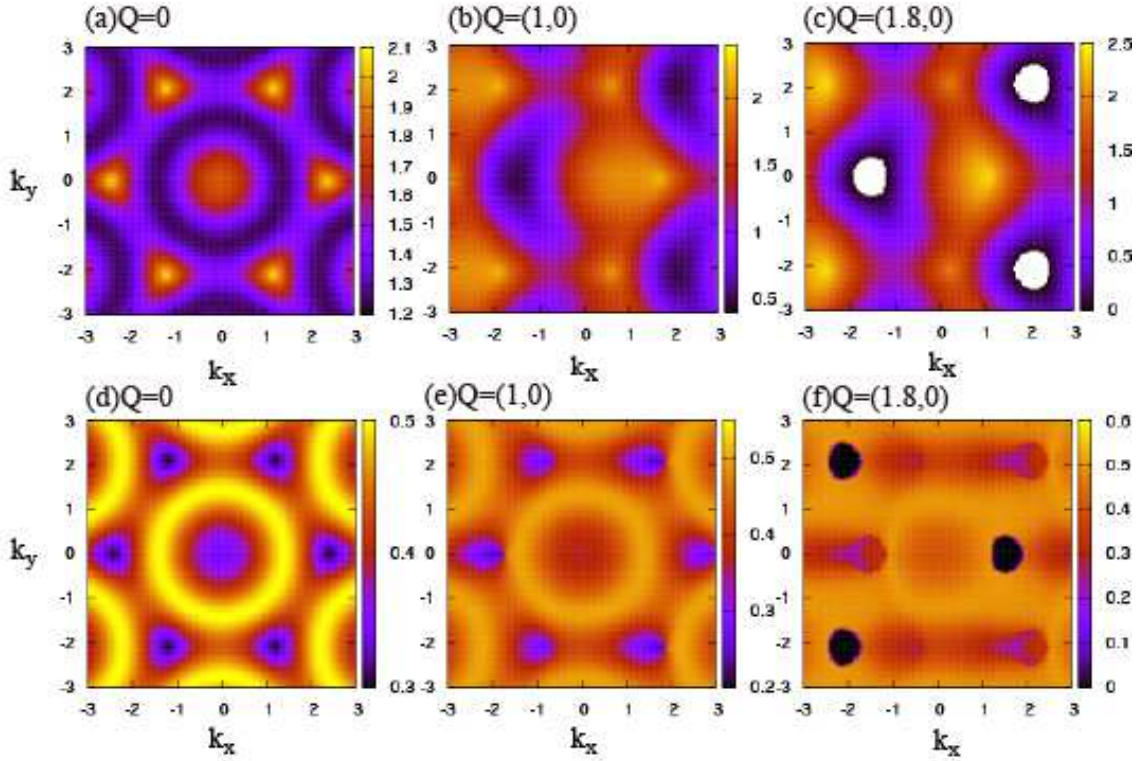


FIG. 5: (Color online) ((a)~(c)) Single-particle spectrum $E_Q^-(\mathbf{k})$ (in units of t) and ((d)~(f)) order parameter weight $w_{Q,A}^-(\mathbf{k})$ (in units of t) in the lower excitation energy band for different flow momenta Q . We set $U/t = 4$, $T = 0$, and $n = 0.5$. In panel (c), $E_Q^-(\mathbf{k})$ takes negative values in the white regions indicating the gapless superfluid state.

However, the closing of the gap does not immediately lead to depairing, as the self-consistent order parameter remains non-zero.

To clarify the origin of this cusp structure, we plot the single-particle spectrum of the lower energy band $E_Q^-(\mathbf{k})$, as well as the order parameter weight for the same band defined as

$$w_{Q,a}^-(\mathbf{k}) \equiv T_{23}^* T_{13} f(E_Q^-(\mathbf{k})) + T_{24}^* T_{14} (1 - f(E_Q^-(-\mathbf{k}))). \quad (14)$$

Here, $f(E) \equiv 1/(e^{\beta E} + 1)$ is the Fermi distribution function and T_{ij} denotes the ij^{th} element of the Bogoliubov transformation matrix in Eq. (9). This quantity $w_{\mathbf{Q},a}^-(\mathbf{k})$ is the contribution from wavevector \mathbf{k} in the gap equation, Eq. (A1). As the quasiparticles are typically gapped, $f(E_{\mathbf{Q}}^-(\mathbf{k})) = 0$ at $T = 0$ and the only contribution to the weight comes from the term proportional to $(1 - f(E_{\mathbf{Q}}^-(\mathbf{k})))$. If the quasiparticle energy becomes negative for a certain momentum \mathbf{p} , i.e., $E_{\mathbf{Q}}^-(\mathbf{p}) < 0$, we have $f(E_{\mathbf{Q}}^-(\mathbf{p})) = 1$. Now, the order parameter weight at $\mathbf{k} = -\mathbf{p}$ - as defined in Eq. (14) - vanishes as $(1 - f(E_{\mathbf{Q}}^-(\mathbf{k}))) = 0$. This is clearly seen in Fig. 5 (c) and (f). The single-particle spectrum becomes gapless at some wavevectors \mathbf{p} , and the order parameter weight vanishes at $-\mathbf{p}$. Thus, the closing of the single-particle gap suppresses the order parameter weight at certain pockets. Consequently, the order parameter decreases sharply subsequently, but remains non-zero. This is the origin of the cusp in Δ vs. \mathbf{Q} at the onset of gapless superfluidity.

IV. COLLECTIVE MODE ANALYSIS

The mean-field theory in Sec. III A describes a superfluid state where Cooper pairs condense in a single momentum state with uniform density. To investigate the stability of superfluid order with imposed flow, we study quantum fluctuations beyond mean-field theory. These fluctuations give rise to dispersing collective modes in the superfluid. For concreteness, we restrict ourselves to flow in the $\Gamma - K$ direction in the rest of this paper. This direction is best suited for the optical lattice setup of Ref. 4 which uses three lasers at angles of 120° with respect to each other. Flow can easily be induced in the $\Gamma - K$ direction by detuning one of the lattice lasers. With this choice of flow direction, given our definition of the unit cell, symmetry forces $\Delta_{\mathbf{Q},a} = \Delta_{\mathbf{Q},b}$.

In general, the collective mode spectrum can be evaluated from the poles of the relevant response functions. In the superfluid state, we have fluctuations in the superfluid order parameter which are coupled to fluctuations in density. Therefore, we calculate the density response function as well as the pair response function. We use the GRPA which treats density and pairing fluctuations on an equal footing. In the context of ultracold Fermi superfluids, GRPA has successfully explained [31] Bragg scattering measurements [32] in the absence of an optical lattice. Various formulations of this method have been used to study the collective modes of Fermi superfluids in deep square/cubic optical lattices [23, 24, 33]. Although GRPA is set up as a weak-coupling perturbation approach, it successfully captures the strong coupling limit as well. Figure 6 shows a comparison of the collective mode dispersion from the GRPA and spin-wave expansion in deep strong-coupling regime ($U/t = 15$). It shows excellent agreement and demonstrates that our GRPA formalism covers from weak-coupling to strong-coupling regime.

In this paper, we present GRPA results based on the Green's function approach developed by Côté and Griffin [34]. For the case of square/cubic lattice, this formulation [24] is in good quantitative agreement with a perturbation theory method used by two of us earlier [23]. For the honeycomb lattice case, we have explicitly checked that these two formulations are also in agreement. We briefly summarize the Côté-Griffin formalism in Appendix B. At strong coupling, we compare GRPA results with spin wave analysis of the appropriate pseudospin Hamiltonian. The formalism of the spin-wave analysis is summarized in Appendix C.

A. Collective modes in the stationary ground state

Figures 7~9 show the dynamic structure factor for density response and pairing response for different values of filling and flow. They are defined, respectively, as

$$S^d(\mathbf{q}, \omega) = -\frac{1}{\pi} \text{Im} \chi_d^{\nu\nu}(\mathbf{q}, i\Omega_n \rightarrow \omega + i\delta), \quad (15)$$

$$S^\Delta(\mathbf{q}, \omega) = -\frac{1}{\pi} \text{Im} \chi_\Delta^{\nu\nu}(\mathbf{q}, i\Omega_n \rightarrow \omega + i\delta). \quad (16)$$

Details are given in the Appendix B. The collective mode spectrum appears as a sharp peak in intensity of either dynamic structure factor, while the broad low intensity region is the two particle continuum.

Since the GRPA equations of motion for the density and pair correlation functions have the same diagrammatic structure (see Eqs. (B14), (B15), and Fig. 12), they share the same poles and therefore collective mode spectrum for coupled fluctuations of density and order parameter phase. However, the spectral weight of the poles can be different for density and pairing correlation functions. The physical origin of collective modes can be understood from the relative weights for density and pairing response. To illustrate this, we discuss collective modes in the stationary ground state ($\mathbf{Q} = 0$) in this section.

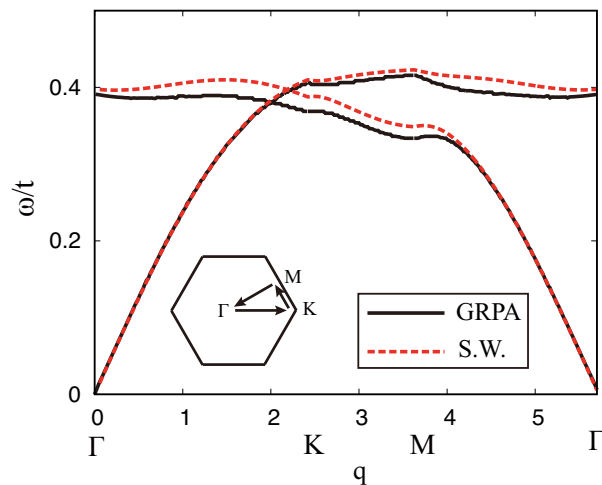


FIG. 6: (Color online) Comparison of the collective mode energy in strong coupling regime ($U/t = 15$) along the contour displayed in the inset. We set $n = 0.5$, $T = 0$, and $\mathbf{Q} = (0.2, 0)$. The GRPA result (solid line) is in good agreement with the spin-wave (S.W.) result (dashed line) for the strong-coupling pseudospin model.

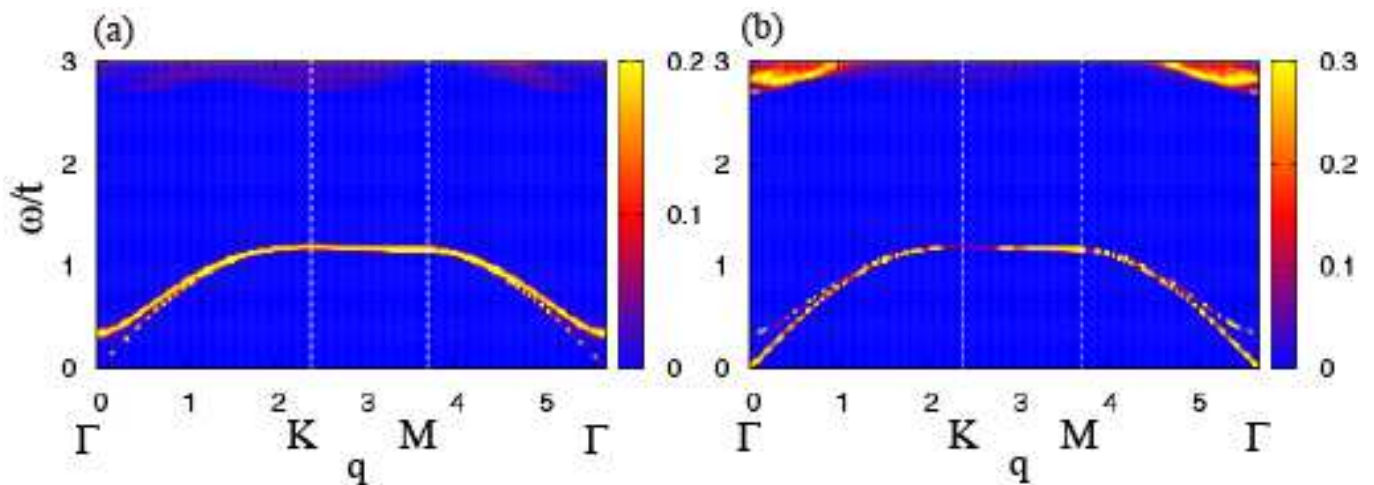


FIG. 7: (Color online) Calculated intensity of the (a) dynamic structure factor of density response function ($S^d(\mathbf{q}, \omega)$) and (b) that of pair response function ($S^\Delta(\mathbf{q}, \omega)$) in the ground state without flow ($\mathbf{Q} = 0$) for $U/t = 4$, $T = 0$, and $n = 0.9$. The momentum \mathbf{q} is along the contour displayed in the inset of Fig. 6. The gapped Leggett mode (see text) has a large density component, while the gapless AB mode has large pairing component.

The honeycomb lattice superfluid can have two undamped collective modes due to the presence of two sites in the unit cell, as shown in Fig. 7:

(i) The lower mode incorporates the gapless Nambu-Goldstone mode corresponding to $U(1)$ symmetry breaking. It is the usual ‘Anderson-Bogoliubov’ (AB) mode, predominantly composed of in-phase pairing fluctuations. This is seen from Fig. 7, where close to the Γ point, the AB mode shows a large intensity of the dynamic structure factor for pairing response.

(ii) The upper mode is a gapped ‘optical’ branch arising from density and/or phase fluctuations which are out of phase between two sublattices. This optical branch can be thought of as a ‘Leggett mode’ [35], in analogy with two-band superconductors such as MgB_2 [36]. When the interaction strength is not too large, as shown in Fig. 9 (d), the Leggett mode may enter the two particle continuum and be strongly damped [14].

Precisely at half-filling, the Hubbard model possesses a special $SU(2)$ pseudospin symmetry [37]. Consequently, the superfluid ground state is degenerate with a CDW state which breaks sublattice symmetry. As a result, the Leggett mode which is composed of out-of-phase density fluctuations, becomes gapless. We are left with two Goldstone modes, as the superfluid state breaks pseudospin $SU(2)$ symmetry and not just $U(1)$ gauge symmetry. Tuning away from half-filling, this degeneracy is weakly broken. The Leggett mode acquires a small gap as shown in Fig. 8 (a)-(d)-(g).

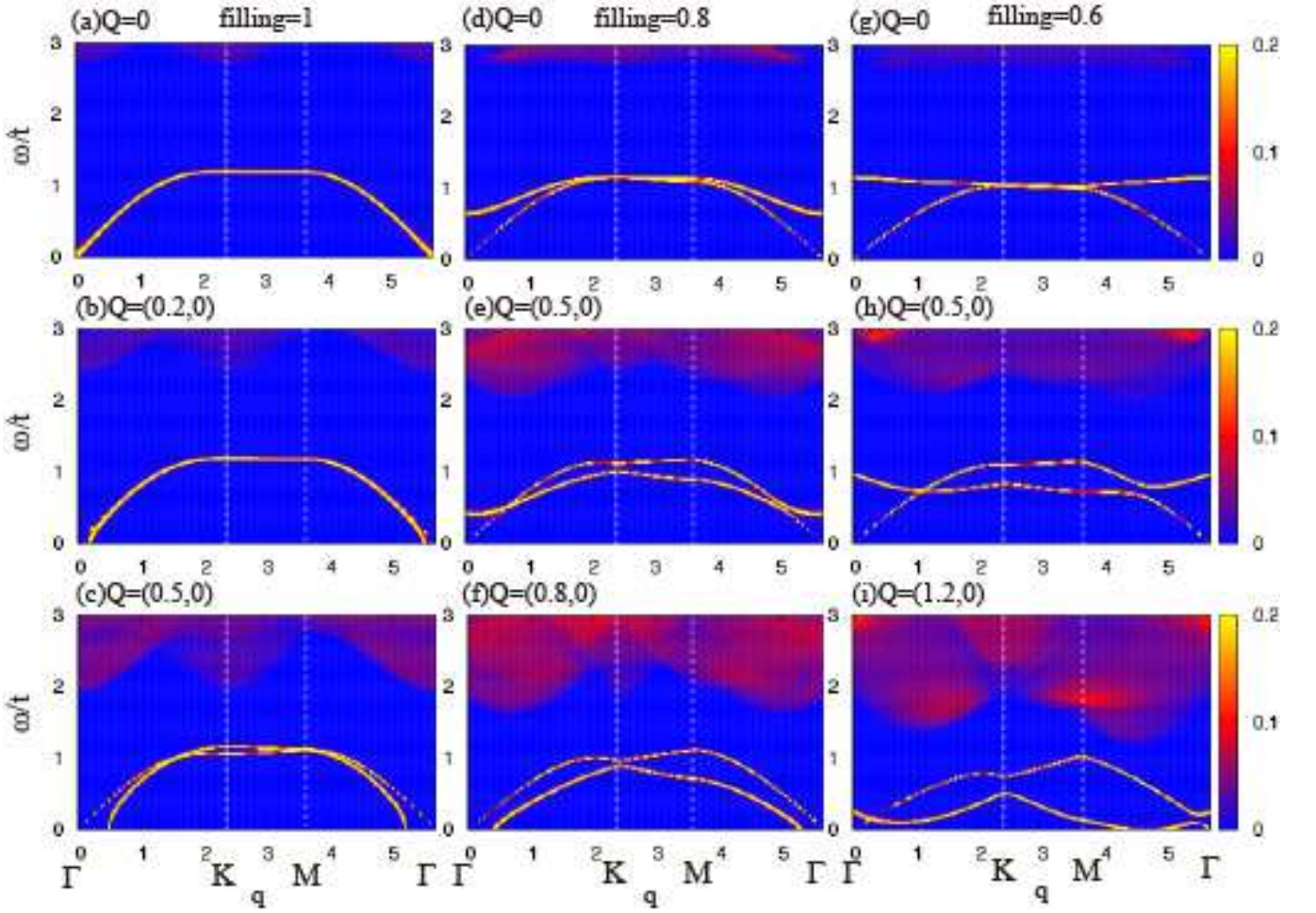


FIG. 8: (Color online) Calculated intensity of the dynamic structure factor of density response function ($S^d(\mathbf{q}, \omega)$) for different fillings and flow momenta, at $U/t = 4$ and $T = 0$. The momentum \mathbf{q} is along the contour displayed in the inset of Fig. 6. The Leggett mode goes down in energy with increasing flow and ‘softens’, signalling an instability.

Close to half-filling, we deduce that the Leggett mode arises from low-lying CDW fluctuations - as shown in Fig. 7, this mode has much larger intensity for density response than for pairing. Far away from half-filling, CDW fluctuations are suppressed and both collective mode branches are predominantly composed of superfluid phase fluctuations.

In addition to these collective modes, there exists a superfluid amplitude mode above the two particle continuum; it appears as a large peak at the edge of continuum in panel Fig. 7 (b). However, this amplitude mode is strongly damped by decay into pairs of single-particle excitations. Consequently, it may prove difficult to detect in experiments. We note that amplitude mode is not coupled with density fluctuations, so that density correlation function does not have such poles and there is no large peak at the edge of the continuum in panel Fig. 7 (a).

B. Superflow instabilities

As described in Sec. III A, we impose superfluid flow on the system by forcing pairing at finite momentum. Superfluidity can be sustained up until some critical flow momentum which is set by one of three possible mechanisms [23]: (I) Depairing instability: the mean-field superfluid order parameter vanishes. As discussed in Sec. III B, this instability occurs at mean-field level for weak to intermediate coupling strengths.

(II) Landau instability: the collective mode energy hits zero and subsequently becomes negative [38]. The negative-energy modes are populated after the onset of the instability, leading to dissipation and the loss of superfluidity. This instability dominates a uniform superfluid Fermi gas in the strong-coupling BEC regime [39].

(III) Dynamical instability: the collective mode dispersion hits zero and subsequently becomes complex-valued. At the onset of this instability, one or more fluctuation modes start growing exponentially. Due to the rapid growth

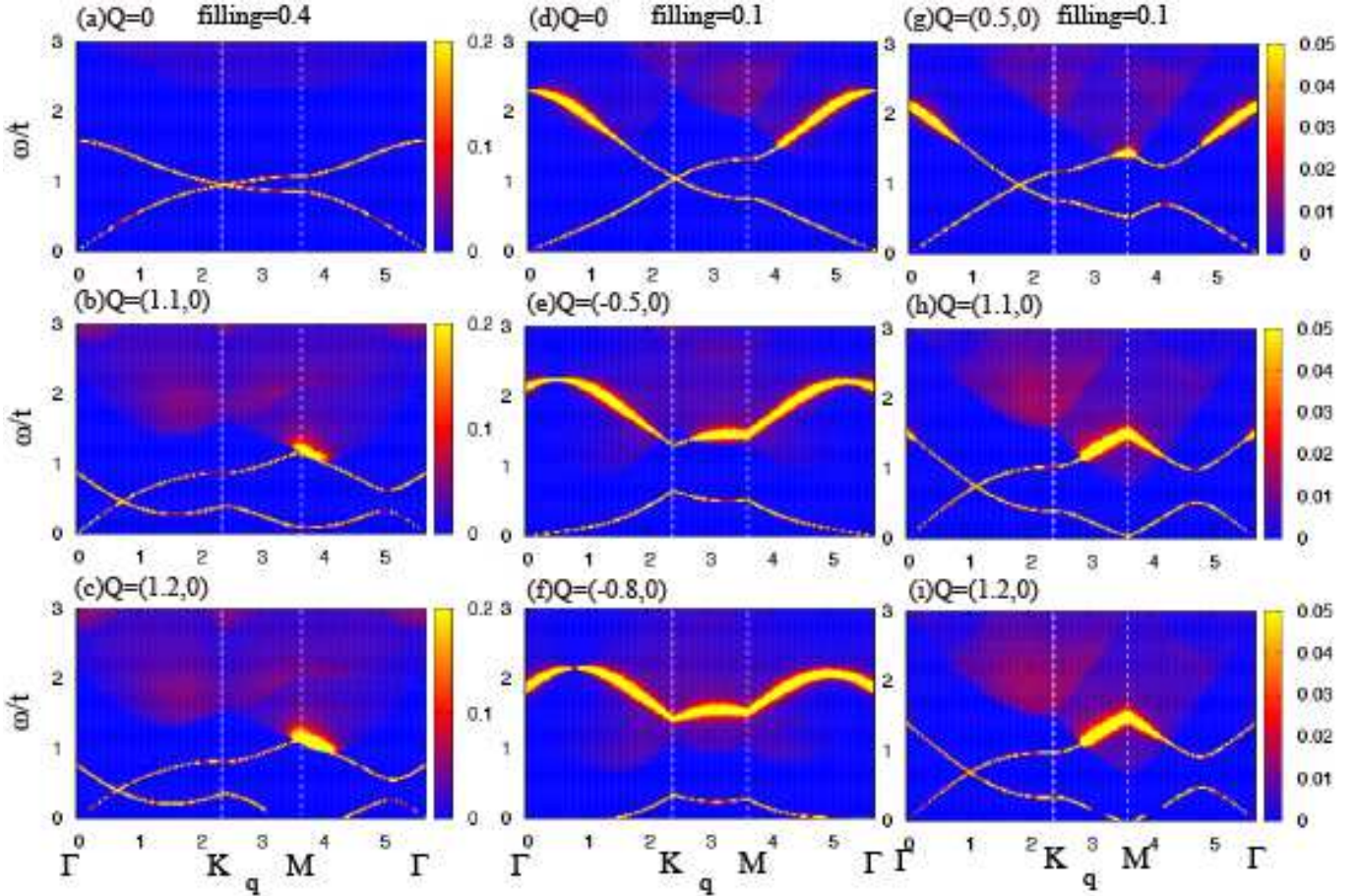


FIG. 9: (Color online) Calculated intensity of the dynamic structure factor of density response function ($S^d(\mathbf{q}, \omega)$) for different fillings and flow momenta, at $U/t = 4$ and $T = 0$. The momentum \mathbf{q} is along the contour displayed in the inset of Fig. 6. The Leggett mode undergoes a dynamical instability at the M point for $n = 0.4$. For $n = 0.1$, the usual Landau instability induced by long wave length AB phonons occurs.

of fluctuations, this instability should be easy to observe in experiments. In fact, dynamical instabilities in bosonic condensates in a 1D optical lattice have been successfully observed [40].

Figures 8 and 9 show the evolution of the collective mode spectrum as imposed flow is increased. As flow is increased, superfluidity is stable until one of the above instabilities occurs. Depending on filling and interaction strength, we can have different leading instabilities. Taking into account all the instabilities and their critical momenta, we map out a superflow ‘stability phase diagram’ in the intermediate coupling regime ($U/t = 4$) (Fig. 10) and strong coupling regime ($U/t = 8$) (Fig. 11 left). We compare the strong coupling phase diagram obtained from GRPA with the one obtained from the spin-wave analysis in the strong coupling regime (Fig. 11 right) - see Appendix C for details.

In the intermediate and strong coupling regimes, the collective mode spectrum always hits zero much before the two particle continuum does (see Figs. 8, 9). When the continuum hits zero, the single-particle spectrum becomes gapless and the system enters the regime of gapless superfluid. As a result, the critical flow momentum is always set by the collective mode as shown in the phase diagram in Fig. 10. The gapless superfluid phase and the depairing instability only exist at mean-field level, and will play no role in experiments. They may become relevant to experiments at weak-coupling strengths. We discuss the instabilities seen in the stability phase diagram below:

Dynamical instability at Γ : In the vicinity of half-filling (see Fig. 8d), the Leggett mode has a small gap. This gap is a measure of the energy difference between the superfluid ground state and the low-lying sublattice-CDW phase. When a finite superflow is imposed, the kinetic energy of superflow overwhelms this excitation energy cost and the system switches to the CDW phase. This manifests itself as the dynamical instability of the Leggett mode at the Γ point. This is shown in panels (d)~(f) of Fig. 8. As flow is increased, the Leggett mode goes down in energy and hits zero at the critical flow momentum. Subsequently, this mode energy becomes complex and sublattice-CDW fluctuations grow exponentially. We see this dynamical instability at the Γ point in the vicinity of and indeed precisely at half-filling (Fig. 8 (a)~(c)).

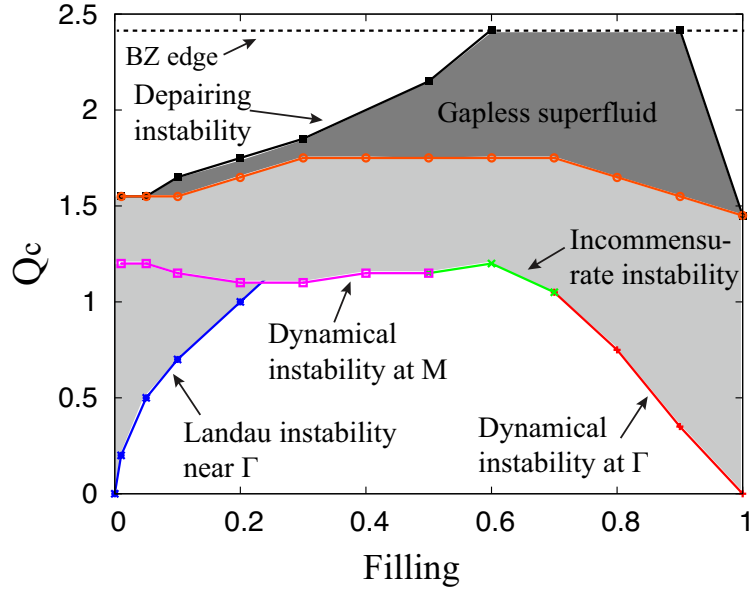


FIG. 10: (Color online) Stability phase diagram for $U/t = 4$. The magnitude of the critical momentum is plotted when the flow is imposed along the x -axis (Γ -K direction). In the light gray region, superfluidity is destroyed by the collective mode instabilities despite of the finite single-particle energy gap. The thick gray region indicates the gapless superfluid region (see text). Note that the depairing instability does not occur for $0.6 \leq n \leq 0.9$ due to the robust superfluidity in the vicinity of the vH singularity at $n = 3/4$.

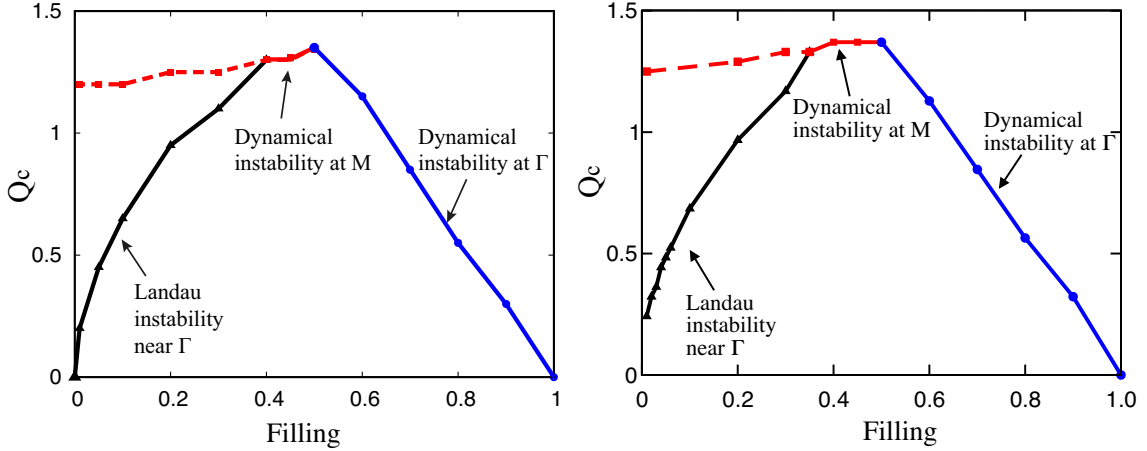


FIG. 11: (Color online) Comparison of the stability phase diagram obtained by the GRPA (left) and spin-wave theory (right) in the strong-coupling regime $U/t = 8$. The magnitude of the critical momentum is plotted when the flow is imposed along the x -axis (Γ -K direction).

Landau instability: At low densities, since the system is similar to a continuum Fermi gas, the leading superflow instability is naturally a Landau instability of AB Goldstone mode. With imposed flow, the AB mode undergoes a ‘Doppler shift’ in the direction opposite to flow and becomes negative at long wavelengths (see panel (d)~(f) in Fig. 9). This type of instability associated with negative energy collective modes has been observed in superfluid fermions in shallow optical lattices leading to the onset of dissipation [39].

Dynamical instability at M : Surprisingly, at intermediate fillings ($n \simeq 0.4$), the leading superflow instability is a dynamical instability of the Leggett mode at the M point (see panels (a)~(c) in Fig. 9). At low densities, this feature persists as a subleading instability occurring beyond the leading Landau instability (see Figs. 11). At low densities, the unstable mode is dominated by phase fluctuations. At intermediate densities, it involves phase and

density fluctuations in roughly equal measure. With our choice of superflow direction (\mathbf{Q} along $\Gamma - K$ direction), this instability occurs at two M points which are symmetric with respect to the flow direction. This instability occurs even when the flow is imposed along the $\Gamma - M$ direction; in which case, only one M point becomes unstable. The nature of the system beyond this instability is an exciting open question - we speculate that either local phase textures will form with local superfluid currents, or that the system will become chaotic.

This M-point instability persists even in the strong coupling limit as shown in Fig. 11. This is in sharp contrast to the square lattice case where only Landau and sublattice-CDW instabilities occur in the strong coupling limit. In the strong coupling regime at low densities, we expect the physics to be dominated by phase fluctuations, captured in a Quantum Rotor (QR) model. In the square lattice case, the QR model is successful in predicting the first *dynamical* instability. This occurs at a flow momentum of $\pi/2$ [41] with the unstable wavevector at the BZ edge centre. On the honeycomb lattice, the QR model predicts a dynamical instability at the flow momentum $\mathbf{Q} = (\pi/\sqrt{3}, 0)$ with the unstable wavevector at the M point. While it gets the wavevector of the instability right, it overestimates the critical flow momentum. Within GRPA and spin wave theory, we find that this instability occurs at $\sim (2\pi/3\sqrt{3}, 0)$. Since density fluctuations are not included in the QR model, they may suppress the critical flow momentum and give rise to the quantitative discrepancy.

Incommensurate dynamical instability: In Fig. 10, the leading instability for intermediate fillings ($0.5 \lesssim n \lesssim 0.7$) at $U/t = 4$ is an incommensurate dynamical instability. This instability can be seen in Fig. 8 (g)~(i) with the unstable wavevector between the Γ and M points. As decreasing filling, the unstable wavevector moves towards the M point. Such an instability does not occur in the strong-coupling regime as shown in Fig. 11. This intermediate-coupling incommensurate instability has also been seen in square/cubic lattices [23, 24].

Figure 11(right) shows the phase diagram in the strong-coupling limit from the spin wave theory. It exhibits qualitatively the same features as the strong-coupling phase diagram obtained by the GRPA in Fig. 11(left): dynamical instability of the Leggett mode at the Γ point around half-filling, Landau instability of the AB mode at low density, and the dynamical instability of the Leggett mode at the M points for intermediate fillings. This demonstrates the consistency of the results obtained in the GRPA and the spin wave analysis and serves as a check for the validity of GRPA.

In addition to the superflow instability discussed above, we remark some characteristic features of the spectra in Figs. 8 and 9. Close to half-filling, the Leggett mode has large component of density fluctuations, while the AB mode is predominantly composed of superfluid phase fluctuations. This is clearly seen in Fig. 8 (e) and (h) as the small level repulsions between the two collective modes in the Γ -M region. At half-filling, the two overlapping peaks of the collective modes in Fig. 8 (b) indicates that they have orthogonal components in fluctuations. On the other hand, at low fillings, since both collective modes are composed of superfluid phase fluctuations, they exhibit large level repulsions in Fig. 9 (b) and (h) in the Γ -M region. We also note that at low densities the Leggett mode as well as the AB mode enters the two particle continuum with small imposed flow in Fig. 9. Consequently, the peaks become broad due to coupling with single-particle states, however, the collective modes still possess high intensity peaks which appear as the bright regions in the continuum.

V. SUMMARY AND DISCUSSION

We have studied the s-wave superfluid state on the honeycomb lattice inspired by recent cold atom experiments. The optical lattice setup of Ref. 6 realizes a honeycomb geometry with tunable anisotropy. Starting from this configuration, we deduce that the symmetric lattice limit is optimal for the study of superfluidity. In addition, superfluidity is most robust at fillings close to $n = 3/4, 5/4$ fermions per site, due to a vH singularity in the non-interacting problem - this is the optimal density for observing superfluidity. Indeed, we find that the highest mean-field T_c^0 at the density corresponding to the vH singularity and in the symmetric lattice case.

The critical velocity superflow is a powerful tool to understand the low-lying excitations of a superfluid. To study this quantity, we first perform a mean-field analysis of the superfluid state while allowing for imposed superflow. Experimentally, superflow can be imposed by using a ‘running’ optical lattice potential. On the honeycomb lattice, we find that superflow generically drives the system into a gapless superfluid state which is widest in the vicinity of the vH singularity at $n = 3/4, 5/4$. Subsequently, the mean-field order parameter vanishes in a first order depairing transition.

We go beyond mean-field theory by including density and pairing fluctuations using the GRPA formalism. At strong coupling, we compare our GRPA results with a spin-wave analysis of the appropriate pseudospin Hamiltonian. Although strictly justified only in the weak-coupling limit, GRPA works well even at strong coupling. We obtain sharp collective mode excitations with two branches - an Anderson-Bogoliubov mode and a Leggett mode. The former incorporates the Goldstone mode from U(1) symmetry breaking. The latter is composed of out-of-phase fluctuations between the two sites of the honeycomb unit cell. At half-filling in the stationary superfluid, this Leggett

mode becomes gapless at the Γ point, due to an extra pseudospin symmetry of the Hubbard model. This arises due to the sublattice-CDW states becoming degenerate with the superfluid. Away from half-filling, the Leggett mode acquires a gap reflecting the energy difference between the superfluid and the CDW.

With imposed superflow, the collective modes come down in energy due to a Doppler shift. An instability occurs when the collective mode softens - subsequently, the mode either becomes negative (Landau instability) or complex-valued (dynamical instability). Close to half-filling, the leading instability is a dynamical instability of the Leggett mode at the Γ point. This instability arises due to competition between the superfluid and sublattice-CDW phases. The presence of the low-lying CDW phase is a special feature of the one-band Hubbard model, arising from a delicate pseudospin rotational symmetry at half-filling. For future experiments, the presence of this instability close to half-filling can serve as a non-trivial test to verify if the one-band Hubbard model has indeed been realized. Naïvely, we may expect this instability to give rise to a stable ‘supersolid’ phase with coexisting superfluid and CDW orders. However, as in the square lattice case [22, 23], the honeycomb system is likely to go into a time-dependent non-equilibrium state. To probe this instability in experiments, it is best to focus on the short time window right after the critical momentum is reached. The exponentially growing CDW correlations can then be probed by rapidly ramping up the optical lattice to freeze the fermion density at each site. Subsequent imaging should give a snapshot clearly showing frozen CDW correlations. Even as we approach the critical flow momentum from below, we can use the same procedure to obtain snapshots which will show CDW fluctuations over some characteristic length scale. This length scale should diverge as we approach the critical flow momentum.

At low densities, we find a Landau instability of the AB mode. We also find an unexpected dynamical instability at the M point for intermediate densities. Surprisingly, this instability persists even at strong coupling. The nature of the system beyond this instability is an interesting open question. We present stability phase diagrams which give the critical flow momentum and the associated instability mechanism as a function of density and interaction strength.

Our calculations are also relevant to recent studies of the *repulsive* Hubbard model on the honeycomb lattice. At half-filling, Quantum Monte Carlo [42] simulations have revealed a gapped spin liquid state at intermediate U/t between semi-metal and Néel phases. There have been many attempts to understand this intermediate phase and the nature of phase transitions into and out of it. Precisely at half-filling, the repulsive and attractive Hubbard models are related by a sublattice-dependent particle hole transformation. In fact, the attractive model at any filling is equivalent to the repulsive problem at half-filling but with a magnetic field [43]. Our GRPA approach does not capture such a strongly correlated phase. However, approaching the spin liquid from the Néel side, the Néel-spin liquid quantum phase transition may arise from melting of Néel order due to collective mode excitations. Such a mechanism has been discussed in Ref.44 in the context of the $\text{Bi}_3\text{Mn}_4\text{O}_{12}\text{NO}(3)$, a spin-3/2 honeycomb lattice antiferromagnet. The question can be phrased within the attractive Hubbard model - can collective modes obtained from GRPA melt superfluid order? If so, what is the nature of the resulting state? This is an interesting direction for future research.

Acknowledgments

S. T. thanks T. Esslinger, M. Sigrist, T. Nikuni, Y. Ohashi, M. Marmorini, D. Yamamoto, and I. Danshita for fruitful discussions. S. T. was supported by Grant-in Aid for Scientific Research, No. 24740276. A. P. was supported by NSERC of Canada.

Appendix A: Mean-field theory equations

The Hamiltonian of Eq. (7) can be solved by a Bogoliubov transformation as given in Eq. (9). Denoting the elements of the transformation matrix T by $(\hat{T})_{ij} = T_{ij}$, the gap equation Eq. (6) gives

$$\begin{aligned} \Delta_{\mathbf{Q},a} = & \frac{U}{M} \sum_{\mathbf{k}} \left[T_{21}^* T_{11} f(E_{\mathbf{Q}}^+(\mathbf{k})) + T_{22}^* T_{12} \left(1 - f(E_{\mathbf{Q}}^+(-\mathbf{k})) \right) \right. \\ & \left. + T_{23}^* T_{13} f(E_{\mathbf{Q}}^-(\mathbf{k})) + T_{24}^* T_{14} \left(1 - f(E_{\mathbf{Q}}^-(-\mathbf{k})) \right) \right], \end{aligned} \quad (\text{A1})$$

$$\begin{aligned} \Delta_{\mathbf{Q},b} = & \frac{U}{M} \sum_{\mathbf{k}} \left[T_{41}^* T_{31} f(E_{\mathbf{Q}}^+(\mathbf{k})) + T_{42}^* T_{32} \left(1 - f(E_{\mathbf{Q}}^+(-\mathbf{k})) \right) \right. \\ & \left. + T_{43}^* T_{33} f(E_{\mathbf{Q}}^-(\mathbf{k})) + T_{44}^* T_{34} \left(1 - f(E_{\mathbf{Q}}^-(-\mathbf{k})) \right) \right], \end{aligned} \quad (\text{A2})$$

where $\langle \alpha_{\mathbf{k},\tau,\sigma}^\dagger \alpha_{\mathbf{k},\tau,\sigma} \rangle = f(E_{\mathbf{Q}}^\tau(\mathbf{k}))$ ($f(E) \equiv 1/(e^{\beta E} + 1)$ is the Fermi distribution function).

The average filling per site n is

$$\begin{aligned}
n &= \frac{1}{2M} \sum_{\mathbf{k}} \sum_{\nu, \sigma} \langle n_{\mathbf{k}, \nu, \sigma} \rangle \\
&= \frac{1}{2M} \sum_{\mathbf{k}} \left[(|T_{11}|^2 - |T_{21}|^2 + |T_{31}|^2 - |T_{41}|^2) f(E_{\mathbf{Q}}^+(\mathbf{k})) \right. \\
&\quad + (-|T_{12}|^2 + |T_{22}|^2 - |T_{32}|^2 + |T_{42}|^2) f(E_{\mathbf{Q}}^+(-\mathbf{k})) \\
&\quad + (|T_{13}|^2 - |T_{23}|^2 + |T_{33}|^2 - |T_{43}|^2) f(E_{\mathbf{Q}}^-(\mathbf{k})) \\
&\quad + (-|T_{14}|^2 + |T_{24}|^2 - |T_{34}|^2 + |T_{44}|^2) f(E_{\mathbf{Q}}^-(-\mathbf{k})) \\
&\quad \left. + |T_{12}|^2 + |T_{14}|^2 + |T_{21}|^2 + |T_{23}|^2 + |T_{32}|^2 + |T_{34}|^2 + |T_{41}|^2 + |T_{43}|^2 \right]. \tag{A3}
\end{aligned}$$

With imposed superflow ($\mathbf{Q} \neq 0$), these equations have to be solved numerically. For the stationary superfluid, however, setting $\Delta_{\mathbf{Q}, a} = \Delta_{\mathbf{Q}, b} = \Delta_0$, the \hat{T} matrix can be obtained analytically.

$$\hat{T}_{\mathbf{Q}=0} = \frac{1}{\sqrt{2}} \begin{pmatrix} e^{i\phi_{\mathbf{k}}} u_{\mathbf{k}}^+ & e^{i\phi_{\mathbf{k}}} v_{\mathbf{k}}^+ & u_{\mathbf{k}}^- & v_{\mathbf{k}}^- \\ -e^{i\phi_{\mathbf{k}}} v_{\mathbf{k}}^+ & e^{i\phi_{\mathbf{k}}} u_{\mathbf{k}}^+ & -v_{\mathbf{k}}^- & u_{\mathbf{k}}^- \\ u_{\mathbf{k}}^+ & v_{\mathbf{k}}^+ & -e^{-i\phi_{\mathbf{k}}} u_{\mathbf{k}}^- & -e^{-i\phi_{\mathbf{k}}} v_{\mathbf{k}}^- \\ -v_{\mathbf{k}}^+ & u_{\mathbf{k}}^+ & e^{-i\phi_{\mathbf{k}}} v_{\mathbf{k}}^- & -e^{-i\phi_{\mathbf{k}}} u_{\mathbf{k}}^- \end{pmatrix}, \tag{A4}$$

where $e^{i\phi_{\mathbf{k}}} = \gamma_{\mathbf{k}}/|\gamma_{\mathbf{k}}|$. The matrix elements $u_{\mathbf{k}}^{\pm}$ and $v_{\mathbf{k}}^{\pm}$ in Eq. (A4) have the standard form as

$$u_{\mathbf{k}}^{\pm} = \sqrt{\frac{1}{2} \left(1 + \frac{\xi_{\mathbf{k}}^{\pm}}{E^{\pm}(\mathbf{k})} \right)}, \quad v_{\mathbf{k}}^{\pm} = \sqrt{\frac{1}{2} \left(1 - \frac{\xi_{\mathbf{k}}^{\pm}}{E^{\pm}(\mathbf{k})} \right)}. \tag{A5}$$

The gap equation (A1) and (A2) reduce to

$$\begin{aligned}
\Delta_0 &= \frac{U}{2M} \sum_{\mathbf{k}} \sum_{\tau=\pm} u_{\mathbf{k}}^{\tau} v_{\mathbf{k}}^{\tau} [1 - 2f(E^{\tau}(\mathbf{k}))] \\
&= \frac{U\Delta_0}{N} \sum_{\mathbf{k}} \sum_{\tau=\pm} \frac{\tanh \frac{\beta E^{\tau}(\mathbf{k})}{2}}{2E^{\tau}(\mathbf{k})}. \tag{A6}
\end{aligned}$$

Thus, we obtain

$$\frac{1}{U} = \frac{1}{N} \sum_{\mathbf{k}} \sum_{\tau=\pm} \frac{\tanh \frac{\beta E^{\tau}(\mathbf{k})}{2}}{2E^{\tau}(\mathbf{k})}. \tag{A7}$$

The number equation (A3) becomes

$$\begin{aligned}
n &= \frac{1}{M} \sum_{\mathbf{k}} \sum_{\tau=\pm} [\{(u_{\mathbf{k}}^{\tau})^2 - (v_{\mathbf{k}}^{\tau})^2\} f(E^{\tau}(\mathbf{k})) + (v_{\mathbf{k}}^{\tau})^2] \\
&= 1 - \frac{1}{N} \sum_{\mathbf{k}} \sum_{\tau=\pm} \frac{\xi_{\mathbf{k}}^{\tau}}{E^{\tau}(\mathbf{k})} \tanh \frac{\beta E^{\tau}(\mathbf{k})}{2}. \tag{A8}
\end{aligned}$$

The above equations (A7) and (A8) have been derived in Ref. [14].

Appendix B: GRPA formalism of Côté and Griffin

In this Appendix, we give a brief summary of the GRPA formalism developed by Côté and Griffin [34]. In this formalism, we introduce fictitious external fields to calculate various response functions by taking functional derivatives of the single-particle Green's function with respect to the external fields. Collective mode spectrum of the system is given by the poles of the response functions. As emphasized in Ref. [34], this technique has the advantage that the response functions are generated by the self-energy approximation for the single-particle Green's function and therefore uniquely determined in consistent with the self-energy approximation.

The Hamiltonian with the time-dependent external fields coupled to density and pair operators is

$$K(\tau) = H + \sum_i P_i(\tau) n_i + \sum_i \left(Q_i^*(\tau) c_{i\uparrow} c_{i\downarrow} + Q_i(\tau) c_{i\downarrow}^\dagger c_{i\uparrow}^\dagger \right), \quad (\text{B1})$$

where τ is imaginary time. Hereafter, we adopt the notation $1 \equiv (j_1, \tau_1) = (l_1, \nu_1, \tau_1)$, where j_1 denotes lattice site, while l_1 and ν_1 denote unit cell and sublattice, respectively. It is convenient to introduce the Nambu representation [45], in which a single-particle Green's function is given in a 2×2 matrix form,

$$\begin{aligned} \hat{G}(1, 2) &= -\langle T \Psi(1) \Psi^\dagger(2) \rangle \\ &= \begin{pmatrix} -e^{-i\frac{\mathbf{Q}}{2} \cdot (\mathbf{r}_{l_1} - \mathbf{r}_{l_2})} \langle T c_{\uparrow}(1) c_{\uparrow}^\dagger(2) \rangle & -e^{-i\frac{\mathbf{Q}}{2} \cdot (\mathbf{r}_{l_1} + \mathbf{r}_{l_2})} \langle T c_{\uparrow}(1) c_{\downarrow}(2) \rangle \\ -e^{i\frac{\mathbf{Q}}{2} \cdot (\mathbf{r}_{l_1} + \mathbf{r}_{l_2})} \langle T c_{\downarrow}^\dagger(1) c_{\uparrow}^\dagger(2) \rangle & e^{i\frac{\mathbf{Q}}{2} \cdot (\mathbf{r}_{l_1} - \mathbf{r}_{l_2})} \langle T c_{\downarrow}(2) c_{\downarrow}^\dagger(1) \rangle \end{pmatrix}. \end{aligned} \quad (\text{B2})$$

The field operator $\Psi(1)$ is a spinor consisting of the creation and annihilation operators

$$\Psi(1) = \hat{\gamma}_{l_1} \begin{pmatrix} c_{\uparrow}(1) \\ c_{\downarrow}(1) \end{pmatrix}, \quad \Psi^\dagger(1) = \begin{pmatrix} c_{\uparrow}^\dagger(1) & c_{\downarrow}(1) \end{pmatrix} \hat{\gamma}_{l_1}^*. \quad (\text{B3})$$

The unitary matrix $\hat{\gamma}_{l_1}$ is given by

$$\hat{\gamma}_{l_1} = \begin{pmatrix} e^{-i\frac{\mathbf{Q}}{2} \cdot \mathbf{r}_{l_1}} & 0 \\ 0 & e^{i\frac{\mathbf{Q}}{2} \cdot \mathbf{r}_{l_1}} \end{pmatrix}. \quad (\text{B4})$$

We note that the Green's function in Eq. (B2) is in the frame fixed to superfluid flow. The Green's function in the lab frame is obtained by the unitary transformation as $\hat{\gamma}_{l_1}^* \hat{G}(1, 2) \hat{\gamma}_{l_2}$.

The Green's function $\hat{G}(1, 2)$ satisfies the Dyson equation

$$[\hat{G}(1, 2)]^{-1} = [\hat{G}^0(1, 2)]^{-1} - \hat{\Sigma}(1, 2) - \hat{W}(1, 2), \quad (\text{B5})$$

where $\hat{G}^0(1, 2)$ is the non-interacting Green's function. The external field matrix $\hat{W}(1, 2)$ is defined as

$$\hat{W}(1, 2) \equiv \delta(1 - 2) \begin{pmatrix} P(1) & -e^{-i\mathbf{Q} \cdot \mathbf{r}_{l_1}} Q(1) \\ -e^{i\mathbf{Q} \cdot \mathbf{r}_{l_1}} Q^*(1) & -P(1) \end{pmatrix}. \quad (\text{B6})$$

The self-energy within the Hartree-Fock-Gor'kov (HFG) approximation is given by

$$\hat{\Sigma}(1, 2) = \delta(1 - 2) \begin{pmatrix} -Un/2 & -\Delta_{\mathbf{Q}, \nu_1} \\ -\Delta_{\mathbf{Q}, \nu_1}^* & Un/2 \end{pmatrix}. \quad (\text{B7})$$

We introduce the three-point *density* correlation function as

$$\hat{L}(1, 2, 3) \equiv \frac{\delta \hat{G}(1, 2)}{\delta P(3)}, \quad (\text{B8})$$

where $\hat{G}(1, 2) \equiv \hat{\tau}_3 \hat{G}(1, 2)$. In the equal space-time limit, it reduces to

$$\hat{L}(1, 3) \equiv \hat{L}(1, 1^+, 3) = \begin{pmatrix} -\langle T \delta n_{\uparrow}(1) \delta n(3) \rangle & -e^{-i\mathbf{Q} \cdot \mathbf{r}_{l_1}} \langle T \delta m(1) \delta n(3) \rangle \\ e^{i\mathbf{Q} \cdot \mathbf{r}_{l_1}} \langle T \delta m^\dagger(1) \delta n(3) \rangle & -\langle T \delta n_{\downarrow}(1) \delta n(3) \rangle \end{pmatrix}. \quad (\text{B9})$$

The density response function is thus obtained from the diagonal elements of Eq. (B9) as

$$\begin{aligned} \chi_d(1, 3) &= \frac{\delta \langle n(1) \rangle}{\delta P(3)} = -\langle T \delta n(1) \delta n(3) \rangle \\ &= L_{11}(1, 3) + L_{22}(1, 3). \end{aligned} \quad (\text{B10})$$

We also introduce the three-point *pair* correlation function as

$$\hat{M}(1, 2, 3) \equiv e^{i\mathbf{Q} \cdot \mathbf{r}_{l_3}} \frac{\delta \hat{G}(1, 2)}{\delta Q(3)}. \quad (\text{B11})$$

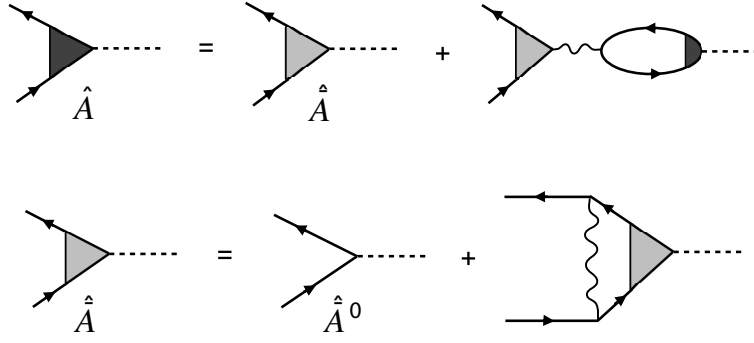


FIG. 12: The diagrammatic representation of the GRPA equations (B14) and (B15). The three point correlation function \hat{A} is either the density (\hat{L}) or pair (\hat{M}) correlation function. The wavy line represents the attractive interaction $-U$. \hat{A} involves the bubble diagrams, while the irreducible correlation function \hat{A} involves the ladder diagrams.

In the equal space-time limit, it reduces to

$$\hat{M}(1, 3) \equiv \hat{M}(1, 1^+, 3) = \begin{pmatrix} -e^{i\mathbf{Q}\cdot\mathbf{r}_{13}} \langle T \delta n_{\uparrow}(1) \delta m^{\dagger}(3) \rangle & -e^{-i\mathbf{Q}\cdot(\mathbf{r}_{11}-\mathbf{r}_{13})} \langle T \delta m(1) \delta m^{\dagger}(3) \rangle \\ e^{i\mathbf{Q}\cdot(\mathbf{r}_{11}-\mathbf{r}_{13})} \langle T \delta m^{\dagger}(1) \delta m^{\dagger}(3) \rangle & -e^{i\mathbf{Q}\cdot\mathbf{r}_{13}} \langle T \delta n_{\downarrow}(1) \delta m^{\dagger}(3) \rangle \end{pmatrix}. \quad (\text{B12})$$

The pair response function is obtained from the off-diagonal element of Eq. (B12) as

$$\begin{aligned} \chi_{\Delta}(1, 3) &= e^{-i\mathbf{Q}\cdot(\mathbf{r}_{11}-\mathbf{r}_{13})} \frac{\delta \langle m(1) \rangle}{\delta Q(3)} \\ &= -e^{-i\mathbf{Q}\cdot(\mathbf{r}_{11}-\mathbf{r}_{13})} \langle T \delta m(1) \delta m^{\dagger}(3) \rangle = M_{12}(1, 3). \end{aligned} \quad (\text{B13})$$

Differentiating $\hat{G}(1, 2)$ with respect to the external fields and using the HFG approximation, one obtains the GRPA equation of motion for the three-point response functions as

$$\hat{A}(1, 2, 5) = \hat{A}(1, 2, 5) - U \int d3 \hat{L}(1, 2, 3) [A_{11}(3, 5) + A_{22}(3, 5)], \quad (\text{B14})$$

$$\hat{A}(1, 2, 5) = \hat{A}^0(1, 2, 5) + U \int d3 \hat{G}(1, 3) \hat{A}(3, 5) \hat{G}(3, 2), \quad (\text{B15})$$

where \hat{A} is either \hat{L} or \hat{M} . The lowest-order correlation functions are given by

$$\hat{L}^0(1, 2, 5) \equiv \hat{G}(1, 5) \hat{G}(5, 2), \quad (\text{B16})$$

$$\hat{M}^0(1, 2, 5) \equiv \hat{G}(1, 5) \begin{pmatrix} 0 & 1 \\ 0 & 0 \end{pmatrix} \hat{G}(5, 2). \quad (\text{B17})$$

$\hat{A}(1, 2, 3)$ is called the irreducible correlation function. The form of Eqs. (B14) and (B15) exposes the diagrammatic structure of the GRPA, as shown in Fig. 12, where Eqs. (B14) and (B15) represent the summation of the ladder diagrams and bubble diagrams, respectively.

The GRPA equations in momentum space are

$$\hat{A}^{\nu_1\nu_2}(q) = \hat{A}^{\nu_1\nu_2}(q) - U \sum_{\nu_3} \hat{L}^{\nu_1\nu_3}(q) A^{\nu_3\nu_2}(q), \quad (\text{B18})$$

$$\hat{A}^{\nu_1\nu_2}(q) = \hat{A}^0{}^{\nu_1\nu_2}(q) + \frac{U}{\beta M} \sum_{\nu_3} \sum_{\mathbf{p}, \omega_n} \hat{G}^{\nu_1\nu_3}(p) \hat{A}^{\nu_3\nu_2}(q) \hat{G}^{\nu_3\nu_1}(p-q), \quad (\text{B19})$$

where $q \equiv (\mathbf{q}, i\Omega_n)$ and $p \equiv (\mathbf{p}, i\omega_n)$ (ω_n and Ω_n are Fermi and Bose Matsubara frequencies, respectively). Here, we defined the Fourier transform as

$$\hat{G}^{\nu_1\nu_2}(1, 2) = \frac{1}{\beta M} \sum_{\mathbf{p}, \omega_n} \hat{G}^{\nu_1\nu_2}(p) e^{i(\mathbf{p}\cdot(\mathbf{r}_{11}-\mathbf{r}_{12})-\omega_n(\tau_1-\tau_2))}, \quad (\text{B20})$$

$$\hat{A}^{\nu_1\nu_2}(1, 2) = \frac{1}{\beta M} \sum_{\mathbf{q}, \Omega_n} \hat{A}^{\nu_1\nu_2}(q) e^{i(\mathbf{q}\cdot(\mathbf{r}_{11}-\mathbf{r}_{12})-\Omega_n(\tau_1-\tau_2))}. \quad (\text{B21})$$

Using Eqs. (B10) and (B13), the density and pair response functions can be evaluated from the correlation functions \hat{L} and \hat{M} that are obtained by solving Eqs. (B18) and (B19).

Appendix C: Spin-wave analysis in the strong coupling limit

In the limit of large U/t , states with singly occupied sites can be ignored leading to an effective spin-1/2 Heisenberg model [23]. The effective Hamiltonian can be written as

$$H = J \sum_{i,\delta=0,-a_2,-a_1-a_2} \mathbf{S}_{i,A} \cdot \mathbf{S}_{i+\delta,B} - (BS) \sum_{i,\alpha} S_{i,\alpha}^z \quad (\text{C1})$$

The exchange interaction $J = 4t^2/U$ arises from superexchange. In this spin mapping, the X and Y directions of spin correspond to the local superfluid order parameter. The density of fermions maps onto the z-polarization, with half-filling mapping to zero z-polarization. The chemical potential in the fermion problem gives rise to a magnetic field tuning polarization. We take the magnetic field to be proportional to S , so that all terms in the Hamiltonian scale as S^2 .

The uniform superfluid state at half-filling maps onto a Néel antiferromagnetic order with spins lying in the XY plane. This state is symmetric under rotation about the Z axis, which corresponds to the usual $U(1)$ gauge symmetry. Superflow is imposed by a phase gradient, which corresponds to twisting the local Néel vector at by an angle $\mathbf{Q} \cdot \mathbf{r}_i$ leading to a spiral state with spins lying in the XY plane. Away from half-filling, a non-zero magnetic field is introduced. This forces the spins to cant uniformly towards the Z axis to gain Zeeman energy. We characterize the flowing superfluid as

$$\begin{aligned} \mathbf{S}_{i,A} &= S(\cos \chi \cos(\mathbf{Q} \cdot \mathbf{r}_i), \cos \chi \sin(\mathbf{Q} \cdot \mathbf{r}_i), \sin \chi) \\ \mathbf{S}_{i,B} &= S(-\cos \chi \cos(\mathbf{Q} \cdot \mathbf{r}_i + \phi), -\cos \chi \sin(\mathbf{Q} \cdot \mathbf{r}_i + \phi), \sin \chi) \end{aligned} \quad (\text{C2})$$

We allow the A and B sublattices to have a relative phase difference ϕ . The Néel state (stationary superfluid) is recovered by setting $\mathbf{Q} = \phi = 0$. For simplicity, we denote the phase angles by $\alpha_i = \mathbf{Q} \cdot \mathbf{r}_i$ and $\beta_i = \mathbf{Q} \cdot \mathbf{r}_i + \phi$. We now perform a local spin rotation and define new spin operators which we denote as $\mathbf{T}_{i,\alpha} = W_{i,\alpha} \mathbf{S}_{i,\alpha}$, by

$$\begin{aligned} \begin{pmatrix} T_{i,A}^x \\ T_{i,A}^y \\ T_{i,A}^z \end{pmatrix} &= \begin{pmatrix} \sin \chi & 0 & -\cos \chi \\ 0 & 1 & 0 \\ \cos \chi & 0 & \sin \chi \end{pmatrix} \begin{pmatrix} \cos(\alpha_i) & \sin(\alpha_i) & 0 \\ -\sin(\alpha_i) & \cos(\alpha_i) & 0 \\ 0 & 0 & 1 \end{pmatrix} \begin{pmatrix} S_{i,A}^x \\ S_{i,A}^y \\ S_{i,A}^z \end{pmatrix}, \\ \begin{pmatrix} T_{i,B}^x \\ T_{i,B}^y \\ T_{i,B}^z \end{pmatrix} &= \begin{pmatrix} -\sin \chi & 0 & -\cos \chi \\ 0 & 1 & 0 \\ \cos \chi & 0 & -\sin \chi \end{pmatrix} \begin{pmatrix} \cos(\beta_i) & \sin(\beta_i) & 0 \\ -\sin(\beta_i) & \cos(\beta_i) & 0 \\ 0 & 0 & 1 \end{pmatrix} \begin{pmatrix} S_{i,B}^x \\ S_{i,B}^y \\ S_{i,B}^z \end{pmatrix}. \end{aligned} \quad (\text{C3})$$

With this local spin rotation, the flowing superfluid state transforms into a uniform antiferromagnet with all spins pointing towards $\pm Z$. We absorb the spin rotation operators into the Hamiltonian. The exchange coupling then takes the form

$$\mathbf{S}_{i,A} \cdot \mathbf{S}_{j,B} = \begin{pmatrix} T_{i,A}^x \\ T_{i,A}^y \\ T_{i,A}^z \end{pmatrix}^T \begin{pmatrix} C_\chi^2 - S_\chi^2 C_{\alpha_i - \beta_j} & S_\chi S_{\alpha_i - \beta_j} & S_{2\chi} C_{(\alpha_i - \beta_j)/2}^2 \\ S_\chi S_{\alpha_i - \beta_j} & C_{\alpha_i - \beta_j} & -C_\chi S_{\alpha_i - \beta_j} \\ -S_{2\chi} C_{(\alpha_i - \beta_j)/2}^2 & C_\chi S_{\alpha_i - \beta_j} & C_\chi^2 C_{\alpha_i - \beta_j} - S_\chi^2 \end{pmatrix} \begin{pmatrix} T_{j,B}^x \\ T_{j,B}^y \\ T_{j,B}^z \end{pmatrix},$$

where $j = i + \delta$. We denote $\sin \theta \equiv S_\theta$ and $\cos \theta \equiv C_\theta$. The Zeeman term in the Hamiltonian becomes

$$-BS(S_{i,A}^z + S_{i,B}^z) = -BS(-C_\chi \{T_{i,A}^x + T_{i,B}^x\} + S_\chi \{T_{i,A}^z - T_{i,B}^z\}). \quad (\text{C4})$$

We now introduce Holstein Primakov bosons as follows:

$$\begin{aligned} T_{i,A}^x &= \sqrt{\frac{S}{2}}(a_i + a_i^\dagger), & T_{i,B}^x &= \sqrt{\frac{S}{2}}(b_i + b_i^\dagger), \\ T_{i,A}^y &= \sqrt{\frac{S}{2}}\left(\frac{1}{i}\right)(a_i - a_i^\dagger), & T_{i,B}^y &= -\sqrt{\frac{S}{2}}\left(\frac{1}{i}\right)(b_i - b_i^\dagger), \\ T_{i,A}^z &= S - a_i^\dagger a_i, & T_{i,B}^z &= b_i^\dagger b_i - S. \end{aligned}$$

The bosonic operators a_i and b_i represent fluctuations about the spiral state. S is the spin length, which we will ultimately set to be $S = 1/2$. The Hamiltonian can now be expanded in powers of S . The leading terms, of order S^2 , give the energy in the classical limit.

$$E_{Cl} = 2NS^2 \left[-JC_\chi^2 \frac{\epsilon_{\mathbf{Q}} e^{i\phi} + \epsilon_{-\mathbf{Q}} e^{-i\phi}}{2} + JS_\chi^2 \epsilon_0 - 2BS_\chi \right], \quad (C5)$$

where N is the total number of sites. Terms proportional to $S^{3/2}$ are linear in boson operators. The coefficient of the single boson operators is complex-valued - we set this quantity to be zero. Setting the real part to be zero, we get

$$\sin \chi = \frac{B}{J(3 + \frac{\gamma_{\mathbf{Q}} e^{i\phi} + \gamma_{-\mathbf{Q}} e^{-i\phi}}{2})}. \quad (C6)$$

Alternatively, this equation be obtained by treating χ as a variational parameter and demanding $\partial_\chi E_{Cl} = 0$. Setting the imaginary part of the coefficient to zero gives

$$\tan \phi = \frac{\sin(Q_2) + \sin(Q_1 + Q_2)}{1 + \cos(Q_2) + \cos(Q_1 + Q_2)}, \quad (C7)$$

where Q_1 and Q_2 are the components of \mathbf{Q} along the primitive vectors \mathbf{a}_1 and \mathbf{a}_2 shown in Fig. 1. This fixes the value of ϕ . Again, this equation can be also obtained variationally by demanding $\partial_\phi E_{Cl} = 0$.

The next terms in the Holstein-Primakov expansion are of order S . These capture the quantum spin wave fluctuations. These terms are given by

$$H_{qu} = 2NS \left[3JS_\chi^2 - JC_\chi^2 \frac{\gamma_{\mathbf{Q}} e^{i\phi} + \gamma_{-\mathbf{Q}} e^{-i\phi}}{2} - BS_\chi \right] + S \sum_k' \psi_{\mathbf{k}}^\dagger H_{\mathbf{k}} \psi_{\mathbf{k}},$$

where

$$\psi_{\mathbf{k}} = \begin{pmatrix} a_{\mathbf{k}} \\ a_{-\mathbf{k}}^\dagger \\ b_{\mathbf{k}} \\ b_{-\mathbf{k}}^\dagger \end{pmatrix}; H_{\mathbf{k}} = \begin{pmatrix} U_{\mathbf{k}} & 0 & X_{\mathbf{k}} + Y_{\mathbf{k}} & Z_{\mathbf{k}} \\ & U_{\mathbf{k}} & Z_{\mathbf{k}} & X_{\mathbf{k}} - Y_{\mathbf{k}} \\ & & U_{\mathbf{k}} & 0 \\ & & & U_{\mathbf{k}} \end{pmatrix}. \quad (C8)$$

As the Hamiltonian matrix is Hermitian, we have only filled in the upper triangle. The entries are given by

$$U_{\mathbf{k}} = J(-3S_\chi^2 + C_\chi^2 \frac{\gamma_{\mathbf{Q}} e^{i\phi} + \gamma_{-\mathbf{Q}} e^{-i\phi}}{2}) + BS_\chi, \quad (C9)$$

$$X_{\mathbf{k}} = \frac{J}{2} \left[C_\chi^2 \gamma_{\mathbf{k}} - (1 + S_\chi^2), \frac{\gamma_{\mathbf{k}+\mathbf{Q}} e^{i\phi} + \gamma_{\mathbf{k}-\mathbf{Q}} e^{-i\phi}}{2} \right], \quad (C9)$$

$$Y_{\mathbf{k}} = -JS_\chi \frac{\gamma_{\mathbf{k}+\mathbf{Q}} e^{i\phi} - \gamma_{\mathbf{k}-\mathbf{Q}} e^{-i\phi}}{2}, \quad (C10)$$

$$Z_{\mathbf{k}} = \frac{J}{2} C_\chi^2 \left[\gamma_{\mathbf{k}} + \frac{\gamma_{\mathbf{k}+\mathbf{Q}} e^{i\phi} + \gamma_{\mathbf{k}-\mathbf{Q}} e^{-i\phi}}{2} \right]. \quad (C11)$$

We obtain the spin wave spectrum by performing a bosonic Bogoliubov transformation on this Hamiltonian matrix. For a given filling and flow momentum, we can thus obtain the collective mode excitations in the strong coupling limit.

-
- [1] I. Bloch, J. Dalibard, and W. Zwerger, Rev. Mod. Phys. **80**, 885 (2008).
[2] T. Esslinger, Annu. Rev. Condens. Matter Phys. **1**, 129 (2010).
[3] A. H. Castro Neto, F. Guinea, N. M. R. Peres, K. S. Novoselov, and A. K. Geim, Rev. Mod. Phys. **81**, 109 (2009).
[4] P. Soltan-Panahi, J. Struck, P. Hauke, A. Bick, W. Plenkers, G. Meineke, C. Becker, P. Windpassinger, M. Lewenstein, and K. Sengstock, Nature Phys. **7**, 434 (2011).
[5] P. Soltan-Panahi, D. Lühmann, J. Struck, P. Windpassinger, and K. Sengstock, Nature Phys. **8**, 71 (2012).
[6] L. Tarruell, D. Greif, T. Uehlinger, G. Jotzu, and T. Esslinger, Nature **483**, 302 (2012).

- [7] F. D. M. Haldane, Phys. Rev. Lett. **61**, 2015 (1988).
- [8] C. L. Kane and E. J. Mele, Phys. Rev. Lett. **95**, 226801 (2005).
- [9] A. Kitaev, Ann. Phys. (N.Y.) **321**, 2 (2006).
- [10] J. L. McChesney, A. Bostwick, T. Ohta, T. Seyller, K. Horn, J. González, and Eli Rotenberg, Phys. Rev. Lett. **104**, 136803 (2010).
- [11] R. Nandkishore, L. S. Levitov, and A. V. Chubukov, Nature Phys. **8**, 158-163 (2012).
- [12] S. Pathak, V. B. Shenoy, and G. Baskaran, Phys. Rev. B **81**, 085431 (2010).
- [13] N. B. Kopnin and E. B. Sonin, Phys. Rev. Lett. **100**, 246808 (2008).
- [14] E. Zhao and A. Paramekanti, Phys. Rev. Lett. **97**, 230404 (2006).
- [15] P. Nikolić and S. Sachdev Phys. Rev. A **75**, 033608 (2007).
- [16] J. K. Chin, D. E. Miller, Y. Liu, C. Stan, W. Setiawan, C. Sanner, K. Xu, and W. Ketterle, Nature **443**, 961 (2006).
- [17] E. G. Moon, P. Nikolic, and S. Sachdev, Phys. Rev. Lett. **99**, 230404 (2007).
- [18] H. Zhai and T. L. Ho, Phys. Rev. Lett. **99**, 100402 (2007).
- [19] A. A. Burkov and A. Paramekanti, Phys. Rev. A **79**, 043636 (2009).
- [20] Y. Prasad, A. Medhi, and V. B. Shenoy, arXiv:1206.2407 (unpublished).
- [21] P. Strack, S. Takei, and W. Metzner, Phys. Rev. B **81**, 125103 (2010).
- [22] A. A. Burkov, A. Paramekanti, Phys. Rev. Lett. **100**, 255301 (2008).
- [23] R. Ganesh, A. Paramekanti, and A. A. Burkov, Phys. Rev. A **80**, 043612 (2009).
- [24] Y. Yunomae, D. Yamamoto, I. Danshita, N. Yokoshi, and S. Tsuchiya, Phys. Rev. A **82**, 033617 (2010).
- [25] S.-L. Zhu, B. Wang, and L.-M. Duan, Phys. Rev. Lett. **98**, 260402 (2007).
- [26] B. Wunsch, F. Guinea, and F. Sols, New J. Phys. **10**, 103027 (2008).
- [27] G. Montambaux, F. Piéchon, J.-N. Fuchs, and M. O. Goerbig, Phys. Rev. B **80**, 153412 (2009).
- [28] D. M. Eagles, Phys. Rev. **186**, 456 (1969).
- [29] A. J. Leggett, *Modern Trends in the Theory of Condensed Matter* (Springer, Berlin, 1980).
- [30] P. Nozières and S. Schmitt-Rink, J. Low. Tem. Phys. **59**, 195 (1985).
- [31] P. Zou, E. D. Kuhnle, C. J. Vale, and H. Hu, Phys. Rev. A **82**, 061605 (2010).
- [32] G. Veeravalli, E. Kuhnle, P. Dyke, and C. J. Vale, Phys. Rev. Lett. **101**, 250403 (2008).
- [33] Z. Koinov, R. Mendoza, and M. Fortes, Phys. Rev. Lett **106**, 100402 (2011).
- [34] R. Côté and A. Griffin, Phys. Rev. B **48**, 10404 (1993).
- [35] A.J. Leggett, Prog. Theor. Phys. **36**, 901 (1966).
- [36] G. Blumberg, A. Mialitsin, B.S. Dennis, M. V. Klein, N. D. Zhigadlo, and J. Karpinski, Phys. Rev. Lett. **99**, 22702 (2007).
- [37] S. C. Zhang, Phys. Rev. Lett. Phys. Rev. Lett. **65**, 120 (1990).
- [38] E. M. Lifshitz and L. P. Pitaevskii, *Statistical Mechanics* (Pergamon, Oxford, 1988), Pt. 2.
- [39] D. E. Miller, J. K. Chin, C. A. Stan, Y. Liu, W. Seitawan, C. Sanner, and W. Ketterle, Phys. Rev. Lett. **99**, 070402 (2007).
- [40] L. Fallani, L. De Sarlo, J. E. Lye, M. Modugno, R. Saers, C. Fort, and M. Inguscio, Phys. Rev. Lett. **93**, 140406 (2004).
- [41] A. Polkovnikov, E. Altman, E. Demler, B. Halperin, and M. D. Lukin, Phys. Rev. A **71**, 063613 (2005).
- [42] Z. Y. Meng, T. C. Lang, S. Wessel, F. F. Assaad, and A. Muramatsu, Nature **464**, 847 (2010).
- [43] A. F. Ho, M. A. Cazalilla, and T. Giamarchi, Phys. Rev. A **79**, 033620 (2009).
- [44] R. Ganesh, D. N. Sheng, Y. J. Kim, A. Paramekanti, Phys. Rev. B **83**, 144414 (2011).
- [45] Y. Nambu, Phys. Rev. **117**, 648 (1958).